Diplomarbeit

Single crystal growth and physical properties of the chiral semimetal CeIrSi

zur Erlangung des Akademischen Grads
Diplom-Ingenieur

im Rahmen des Studiums
Technische Physik

ausgeführt am Institut für Festkörperphysik
der Fakultät für Physik an der Technisch Universität Wien

unter der Anleitung von
Associate Prof. Dipl.-Chem. Dr.rer.nat. Andrey Prokofiev
Dr.rer.nat. Xinlin Yan

durch
Maurice Michael Naessens, BSc.
Matr.-Nr.: 11916289

Wien, 09 Mai 2025 _____ _____

Unterschrift Verfasser Unterschrift Betreuer

Abstract

Weyl-Kondo semimetals are materials in which strong electron correlations and non-trivial electronic topology are combined. In these materials, the quasiparticles - Weyl fermions - have a linear dispersion relation, making them an analogue of relativistic massless particles. Candidate materials must have a crystal structure with broken inversion symmetry or time-reversal symmetry. New aspects of Weyl fermion physics are expected in crystals of even lower symmetry, in chiral crystals. A candidate for Kramers Weyl Kondo semimetal CeIrSi was found based on its chiral structure (space group $P2_13$, N198), strong spin-orbit coupling and signatures of strong electron correlations in heat capacity. High-quality, stoichiometric single crystals were successfully grown for the first time using the optical floating zone method and subsequently used for magnetization (up to 6 T), heat capacity, and electrical transport measurements (up to 12 T) along the crystallographic directions [100] and [110] over a temperature range from room temperature down to 2 K. Heat capacity measurements revealed an enhanced Sommerfeld coefficient, indicating strong electronic correlations, while resistivity exhibited a strong anisotropic behaviour, showing semimetallic character along [100] and semiconducting behaviour along [110]. The material is paramagnetic down to 8 K, however, in contrast to the literature, which reports it as non-magnetic, at least three different magnetically ordered phases were found below 8 K. At magnetic fields above 3.7 T, the compound behaves like a collinear ferromagnet. Below this field, two different magnetic phases 1 and 2 with ferromagnetic and antiferromagnetic features appear, possibly conical and helical in nature, but their exact structure is still unclear and requires further investigation. Hall effect measurements between 2 K and 8 K show a strong non-linear contribution, which cannot be easily attributed to intrinsic effects from the Berry curvature. It may arise from complex magnetic ordering at low temperatures. Therefore, further measurements are needed to clarify the complex magnetic ordering and to determine the topological contributions to the strong non-linear Hall effect.

Zusammenfassung

Weyl-Kondo-Semimetalle sind Materialien, in denen starke Elektronenkorrelationen und nicht-triviale elektronische Topologie kombiniert sind. In diesen Materialien haben die Quasiteilchen – Weyl-Fermionen – eine lineare Dispersion, was sie zu einem Analogon relativistischer masseloser Teilchen macht. Potentielle Materialien müssen eine Kristallstruktur mit gebrochener Inversionssymmetrie oder Zeitumkehrsymmetrie aufweisen. In Kristallen mit noch geringerer Symmetrie, insbesondere in chiralen Kristallen, werden neue Facetten der Weyl-Fermionenphysik erwartet. Ein Kandidat für ein Kramers Weyl Kondo Semimetall, CeIrSi, wurde aufgrund seiner chiralen Struktur (Raumgruppe $P2_13$, N198), starken Spin-Bahn-Kopplung und Hinweise starker Elektronenkorrelationen in der Wärmekapazität gefunden. Zum ersten mal wurden hochwertige, stöchiometrische Einkristalle erfolgreich mittels der optischen Floating-Zone-Methode gezüchtet und anschließend für Magnetisierungsmessungen (bis 6 T), Wärmekapazitätsmessungen sowie elektrische Transportmessungen (bis 12 T) entlang der kristallographischen Richtungen [100] und [110] im Temperaturbereich von Raumtemperatur bis 2 K verwendet. Wärmekapazitätsmessungen offenbaren einen erhöhten Sommerfeld-Koeffizienten, der auf starke elektronische Korrelationen hindeutet. Gleichzeitig zeigt der Widerstand ein deutlich anisotropes Verhalten: Entlang der Richtung [100] tritt semimetallisches Verhalten auf, während entlang [110] ein halbleitendes Verhalten beobachtet wird. Das Material ist bis 8 K paramagnetisch, jedoch sind im Gegensatz zur Literatur, die es als nicht-magnetisch beschreibt, mindestens drei verschiedene magnetisch geordnete Phasen unterhalb von 8 K gefunden worden. Bei Magnetfeldern über 3.7 T verhält sich die Verbindung wie ein kollinearer Ferromagnet. Unterhalb dieses Feldes treten zwei verschiedene magnetische Phasen 1 und 2 mit ferromagnetischen und antiferromagnetischen Anteilen auf, möglicherweise konischer und helikaler Natur, deren genaue Struktur jedoch ohne weitere Untersuchungen nicht eindeutig identifiziert werden können. Hall Effekt Messungen im Bereich von 2 K bis 8 K zeigen einen starken nichtlinearen Beitrag, der nicht einfach den intrinsischen Effekten der Berry Krümmung zugeordnet werden kann. Stattdessen, könnte dieser auch durch die komplexe magnetische Ordnung bei niedrigen Temperaturen entstehen. Folglich sind weitere Messungen erforderlich, um die komplexe magnetische Ordnung zu klären und die topologischen Beiträge zum starken nichtlinearen Hall-Effekt zu bestimmen.

Contents

1 Introduction

Strongly correlated systems are defined by the presence of significant electron–electron interactions, where the Coulomb repulsion is comparable to or even larger than the kinetic energy of the electrons [1]. A prominent class within these systems are heavy fermion compounds, often found among intermetallic materials that contain rare-earth elements. These elements host localized magnetic moments originating from $4f$ or $5f$ electrons. Heavy fermion systems are characterized by extremely flat electronic bands, which result in a dramatically enhanced effective electron mass. One particularly intriguing aspect of these systems is the competition between a non-magnetic ground state, arising from Kondo screening, and a magnetically ordered state favoured by the Ruderman–Kittel–Kasuya–Yosida (RKKY) interaction. Especially at low temperatures, where both effects may coexist, this competition can give rise to complex magnetic phenomena and non-Fermi-liquid behaviour. [2].

In the last decades, a new class of topological materials has garnered significant attention in condensed matter physics. Among these, topological insulators, Dirac semimetals, and Weyl semimetals have emerged as key players in the study of exotic electronic states, owing to their rich variety of exotic phases. These materials exhibit unique and highly non-trivial topological properties, which give rise to new quantum states such as Fermi arcs [1, 3, 4]. In 2015, the first Weyl fermions were discovered in the strong spin-orbit coupled material TaAs, where fermi arcs were observed using angle-resolved photoemission spectroscopy (ARPES) [5]. In materials with broken inversion and/or time-reversal symmetry, Weyl points of opposite chirality emerge from band inversion. These Weyl points, respresented by the Berry curvature field, can be described by massless chiral fermions [3, 6, 7]. In addition to the surface states, the Berry curvature field influences transport properties. The sources and sinks of the Berry curvature (the Weyl nodes) behave like fictitious magnetic monopoles, leading to pronounced contributions in Hall effect measurements. These contributions will serve as a central experimental approach for identifying topological electronic states in this thesis [8, 9].

In the absence of certain crystal symmetries, as found in chiral crystals, a new class of Weyl fermions, known as Kramers-Weyl fermions, has emerged. Kramers-Weyl semimetals are characterized by large, non-trivial topological energy windows and are known to host large Fermi arcs, as observed in RhSi [10]. Moreover, these materials exhibit unusual

phenomena such as the chiral anomaly and the circular photogalvanic effect (CPGE) [4]. They originate from band degeneracies that are lifted throughout the Brillouin zone, except at time-reversal invariant momentum points (TRIMs) in chiral crystals, which leads to Kramers-Weyl points that are maximally separated in momentum space [4, 11].

So far, the investigation of Kramers-Weyl fermions has primarily focused on non-interacting systems and those with weak electronic correlations. However, it is anticipated that strong correlations, in combination with spin-orbit interactions and special space group symmetries, may give rise to a rich variety of topological states of matter, analogous to Weyl-Kondo semimetals, such as $Ce_3Bi_4Pd_3$ [1, 6]. In this work, we investigate CeIrSi as a candidate for a Kramers-Weyl Kondo semimetal, distinguished by its chiral crystal structure, strong spin-orbit coupling required to lift band degeneracies, and signatures of strong electronic correlations.

Previous studies of polycrystalline samples revealed that this compound crystallizes in the cubic chiral space group 198 - $P2_13$ [12, 13], which is known to host Weyl fermions with high Chern numbers, resulting in strong topological protection [14]. While the single crystal growth of CeIrSi is unexplored, polycrystalline samples of have been reported to be non-magnetic down to temperatures as low as 300 mK, exhibiting a semiconducting temperature dependence. This makes CeIrSi a promising candidate, together with materials containing the heavy element iridium often exhibit strong spin-orbit coupling, and the rare earth element Ce is known to support heavy fermion systems, such as $CeAl_3$ [15].

This thesis presents the procedure for the single crystal growth of CeIrSi, as well as investigations on its physical properties, including magnetization, thermal and electrical transport, as well as Hall effect measurements, to identify any topological contributions from room temperature to 2 K. The following chapter discusses the theoretical models essential for understanding these results.

2 Theoretical background

The following section provides an overview of the physical concepts and interactions relevant to understanding the phenomena observed in strongly correlated electron systems and materials exhibiting topological states of matter, such as Weyl semimetals. Special emphasis is placed on the Kondo effect and RKKY interactions, which commonly arise in systems containing rare-earth elements, such as Ce with $4f$ electron configurations. The concept of Kramers-Weyl semimetals is introduced in the context of CeIrSi, a chiral compound proposed as a promising candidate in this emerging class of topological materials, where spin-orbit coupling and structural chirality play a central role. The chapter concludes with a discussion of Hall effect measurements as a powerful tool for probing topological materials, and the importance of high-quality single crystal growth to enable precise and reliable experimental investigations.

2.1 Weyl semimetal (WS)

Weyl fermions were first introduced in 1929 as an alternative solution to the Dirac equation, alongside the known Dirac fermions, for relativistic particles in high-energy physics. The mathematician Herman Weyl predicted the existence of massless fermions characterized by a well-defined chirality, which are described by a two-component spinor that satisfies the Weyl equation [3, 16, 17]. Despite this theoretical foundation, Weyl fermions have yet to be experimentally identified in particle physics. In contrast, the concept has been extended in the context of quantum materials to describe topological fermions.

In a Dirac semimetal, two degenerate bands (the conduction and valence bands) touch at discrete points known as Dirac points (see Fig. 2.1) [7]. These points exhibit linear dispersion in all three momentum directions [3, 7, 18]. As a result, the low-energy quasiparticle excitations behave as massless Dirac fermions.

If inversion symmetry (IS) and/or time-reversal symmetry (TRS) is broken, a Dirac point splits into two non-degenerate Weyl points with opposite chirality (see Fig. 2.1)[3].

The Weyl points are represented as sources and sinks of the Berry curvature field $\overrightarrow{\Omega_m}(\vec{k})$ in momentum space $\vec{k}$. To maintain neutrality within the Brillouin zone, Weyl points

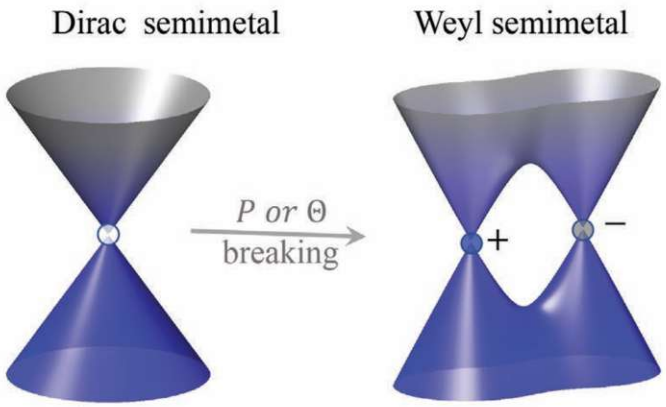

Figure 2.1: Degenerate Dirac points with linear dispersion in momentum space transform into doubly degenerate chiral fermions of opposite charge when either IS or TRS is broken. Adapted from Ref. [7].

always appear in pairs of opposite charge, as dictated by the Nielsen-Ninomiya no-go theorem [7].

The integral of the Berry curvature field (Eq. 1) over a surface S that encloses a Weyl point yields a quantized integer Chern number C_m, which serves as the topological invariant associated with the Weyl fermion and defines its topological charge.

$$C_m = \frac{1}{2\pi} \int_S \overrightarrow{\Omega_m}(\vec{k}) d\vec{S} \tag{1}$$

whereas the Berry curvature is given by

$$\overrightarrow{\Omega_m}(\vec{k}) = \nabla_{\vec{k}} \times \overrightarrow{A_m}(\vec{k}) \tag{2}$$

with the Berry connection $\overrightarrow{A_m}(\vec{k})$ which describes how the phase of a quantum state evolves as the system undergoes adiabatic changes in parameter space.

In simpler terms, the Weyl points emerge from a band inversion where the conduction band drops below the valence band in energy, creating a non-trivial topological energy window (see Fig. 2.2a). Within this topological window, protected surface states manifest themself as Fermi arcs (see Fig. 2.2b).

Typically, the Fermi surface forms closed loops in momentum space, however, in Weyl semimetals, these loops transform into arcs. These unique surface states can be detected using angle-resolved photoemission spectroscopy (ARPES), as demonstrated in the case of TaAS [5], which was the first Weyl semimetal identified in 2015.

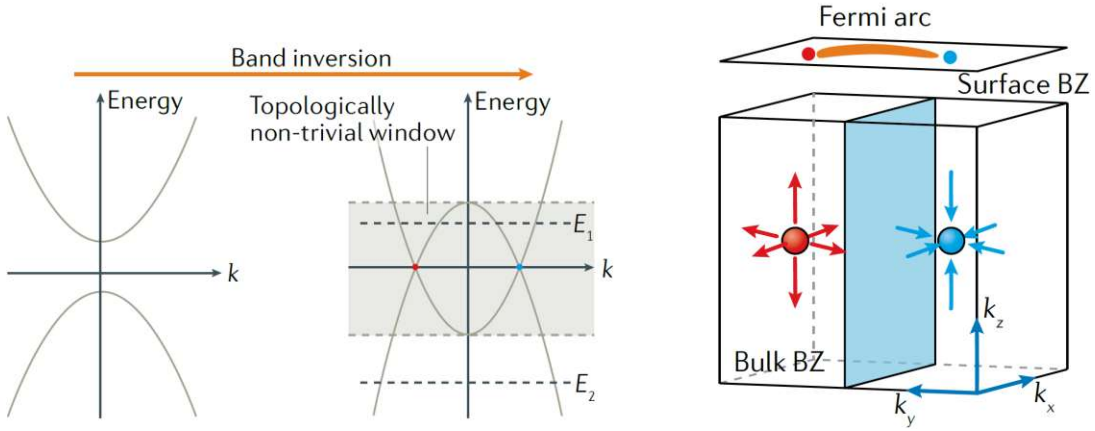

(a) (b)

Figure 2.2: a) Weyl fermions generated by band inversion in crystals breaking IS or TRS. The extrema of the bands give the limits of the topological non-trivial energy window. b) Illustration of two chiral Weyl fermions in the bulk Brillouin zone (BZ) and the Fermi arc in the surface of the BZ. Adapted from Ref. [3]

In addition to surface states, the Berry curvature field influences transport properties, as the sources and sinks of Berry curvature (the Weyl nodes) behave like fictitious magnetic monopoles. Research over the past decade has demonstrated that spontaneous Hall effect measurements are an effective method for detecting these Weyl nodes (see section 2.7) [6, 8, 9].

Weyl points exist exclusively within a finite topological energy window, which is mainly determined by the degree of band inversion. A greater degree of band inversion leads to a larger separation between Weyl points, thereby enhancing the stability of a robust topological phase. However, studying topological phenomena can be challenging, as the Fermi level often lies outside of the topolgical energy window [3].

Band inversion is a key criterion in the identification of potential topological material candidates. In particular, in rare-earth materials, the strong spin-orbit coupling plays a crucial role in driving band inversion [19].

2.2 Kondo effect

Strongly correlated heavy fermion systems are characterized by significant interactions between localized magnetic moments (often associated with $4f$ or $5f$ electrons) and con-

duction electrons. The foundational model for these interactions is the Kondo effect [2], first explained by J. Kondo 60 years ago. In the early research phase of condensed matter systems, W. J. de Haas, J. de Boer, and G.J. van den Berg discovered an unexpected rise in the resistivity of magnetic impure gold wires at low temperatures in 1934. At that time, total electric resistivity was attributed to electron scattering from phonons (lattice vibrations) and impurities, following Matthiessen's rule. While theoretical predictions and experimental observations aligned for simple metals, they could not account for the anomalous resistivity behaviour observed in gold wires. J. Kondo addressed this by incorporating electron scattering on magnetic impurities into his model, utilizing perturbation theory based on the *s*-*d* model developed by Anderson. He considered not only first-order but also second-order scattering processes, including spin flips. Consequently, localized $4f$ or $5f$ electrons from impurities can transition into the continuum and exchange their orbital and spin quantum numbers through intermediate states, accompanied by electron-hole excitations, commonly referred to as quasiparticle excitations in Landau's Fermi-liquid theory. The contributions to the total energy can be described using the Heisenberg model, accounting for both energy and spin changes as follows:

$$H = -J(\vec{r})\vec{\sigma} \cdot \vec{S} \tag{3}$$

where $J(\vec{r})$ is the exchange coupling parameter ($J < 0$ for antiferromagnetic and $J > 0$ for paramagnetic interactions), $\vec{\sigma}$ represents the spin component of the conduction electrons, and $\vec{S}$ denotes the localized moment of the impurity.

By considering spin exchanges between conduction electrons and the localized moment, an additional term proportional to $J^3 \log T$ emerges, which accounts for the observed logarithmic increase in electrical resistivity as temperature decreases (see Fig. 2.4) for negative exchange coupling (i.e., antiferromagnetic, $J < 0$). The perturbation theory breaks down as $T \to 0$ due to the divergence of this logarithmic term, a phenomenon known as the *Kondo problem*.

To deal with the unphysical divergence of several physical quantities, Abrikosov extended perturbation theory to a general n-th order approach and successfully summarised the leading logarithmic terms at low temperatures. However, it was found that the resistivity for antiferromagnetic interactions diverges at finite temperatures T_K.

$$k_B T_K \approx D \exp\left(-\frac{1}{2|J|N(E_F)}\right) \tag{4}$$

with the Boltzmann factor k_B, the bandwidth D of the conduction electrons and $N(E_F)$

representing the density of states of the conduction electrons at the Fermi energy.

The characteristic Kondo temperature T_K defines the crossover between weak ($T > T_K$) and strong ($T < T_K$) correlations. Below the Kondo temperature, conduction electrons couple strongly with the spin of the impurity moments. Furthermore, the spins of the conduction electrons align anti-parallel with the spin of the impurity. Hence, the magnetic moment seems to be screened by the conduction electrons, forming a non-magnetic singlet ground state (see Fig. 2.3), with an energy gain of $k_B T_K$ in comparison to the magnetic triplet state. As the magnetic impurity can no longer be seen by the conduction electrons, the unphysical divergence vanishes, and the resistivity saturates for $T \to 0$ (see Fig. 2.4).

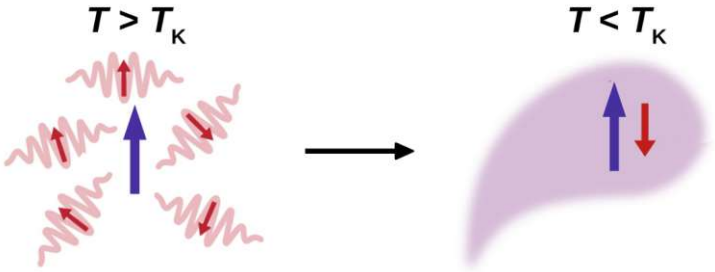

Figure 2.3: Below the Kondo temperature, the system enters the strong coupling regime, where conduction electrons strongly couple with the impurity to form a screening cloud. Adapted from reference [2]

The formation of a singlet ground state at low temperatures modifies the electronic density of states (DOS) near the Fermi energy. An additional peak $\rho_f(\omega)$ with a large DOS appears to compensate for the loss of spin degree of freedom. This peak is responsible for unusual behaviour at low temperatures, as well as the enhanced effective mass of electrons, and is known as the *Kondo resonance* with a width of $k_B T_K$ (Fig. 2.5a & 2.5b).

Mainly adapted from reference [2].

2.2.1 Kondo lattice

In the case of a periodic arrangement of localized magnetic moments, known as a *Kondo lattice*, the magnetic ions decouple above the Kondo temperature T_K, resulting in behaviour characteristic of the single-ion Kondo effect. In contrast, within the Kondo coherence regime below T_K, the electrical resistivity decreases (Fig. 2.4), as the conduction

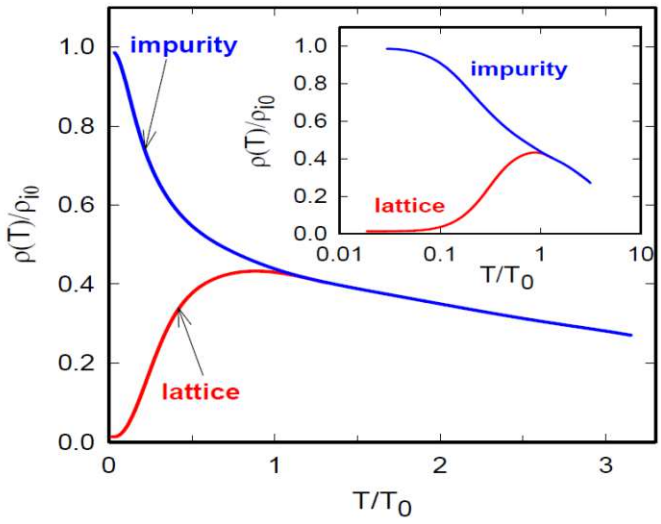

Figure 2.4: The typical low-temperature resistivity behaviour for the single-ion and lattice Kondo effect. Adapted from Ref. [2].

electrons can pass through the periodic scattering centers in the form of Bloch waves.

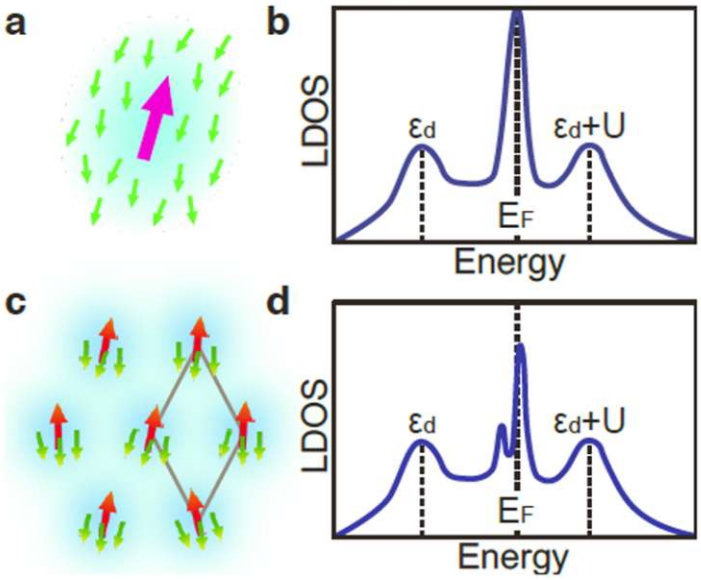

Figure 2.5: a) Single impurity: Spin of the impurity (pink) in the sea of the spins of the conduction electrons. b) The local density of states (LDOS) associated with panel a. c) Kondo lattice created from a series of impurities d) The LDOS corresponding to panel c. In panels b and d, ϵ_d denotes the energy level of the singly occupied electronic state of the impurity, while $\epsilon_d + U$ indicates the energy required for double occupancy of that state. Adapted from Ref. [20].

The hybridization of the localized (mostly) f-electrons with the conduction electrons cre-

ates a partial hybridization gap in the density of states at the Fermi energy (see Fig. 2.5d).

Since the effective mass of the electrons is proportional to the density of states, this results in the formation of a flat band of heavy quasiparticles with a width of $k_B T_K$. Consequently, these systems are often referred to as *heavy fermion systems*.

The periodic arrangement of the Kondo scattering centers, along with the resulting demagnetized ground state, leads to a T^2 dependence of the electrical resistivity

$$\rho(T) = \rho_0 + AT^2 \tag{5}$$

with the prefactor A and the residual resistance ρ_0 that arises from the scattering of impurities and defects.

2.2.2 Ground state competition

In the Kondo lattice, the magnetic moments are effectively screened by the conduction electrons, leading to a non-magnetic ground state. However, in this periodic arrangement of magnetic moments, long-range intersite interactions, such as the RKKY interaction (Rudermann, Kittel, Kasuya, Yoshida), become significant. This interaction represents an indirect coupling between localized magnetic moments that is mediated by conduction electrons. The screening of these localized moments induces a spin polarization in the conduction electrons. As a result, neighbouring magnetic ions adjust their moments in response to this spin polarization. Due to the oscillatory nature of the RKKY interaction (Eq. 6), the response can be either negative (antiferromagnetic) or positive (ferromagnetic), depending on the ion distance r. This behaviour is depicted by the RKKY exchange relation shown in (Fig. 2.6).

$$J_{RKKY} \propto J^2 N(E_F) \frac{x\cos x - \sin x}{x^4} \tag{6}$$

where $x = 2k_F r$ and $k_F \equiv$ represents the Fermi wavevector.

The favourable formation of a compensated spin state or magnetic order, which is primarily influenced by the RKKY interaction, hinges on the exchange integral $|JN(E_F)|$. The strength of the Kondo interaction is characterized by an exponential dependence:

$$T_K \propto \exp\left(-1/|JN(E_F)|\right)$$

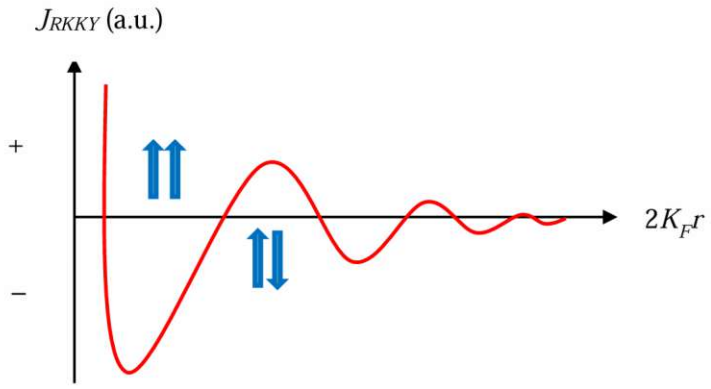

Figure 2.6: Oscillating RKKY interaction with positive or negative exchange coupling Parameter. Adapted from Ref. [21].

In contrast, the RKKY interaction exhibits a quadratic dependence:

$$T_{RKKY} \propto |JN(E_F)|^2$$

For small values of J, the relationship $T_{RKKY} > T_K$ holds due to the exponential nature of the Kondo interaction (see Fig. 2.7). This condition favours the emergence of a magnetically ordered ground state. However, for large values of J, the energy gain associated with singlet formation becomes dominant compared to that of a magnetically ordered state. Even when lowering the temperature below the Kondo temperature, achieving an ordered state becomes impossible because the magnetic moments are already screened by conduction electrons [22].

At the critical point J_c, where $T_K \approx T_{RKKY}$, both interactions can coexist simultaneously, leading to intriguing magnetic phenomena. Near this quantum critical point (QCP) at $(T = 0)$, non-Fermi liquid behaviour emerges as a result of strong spin fluctuations.

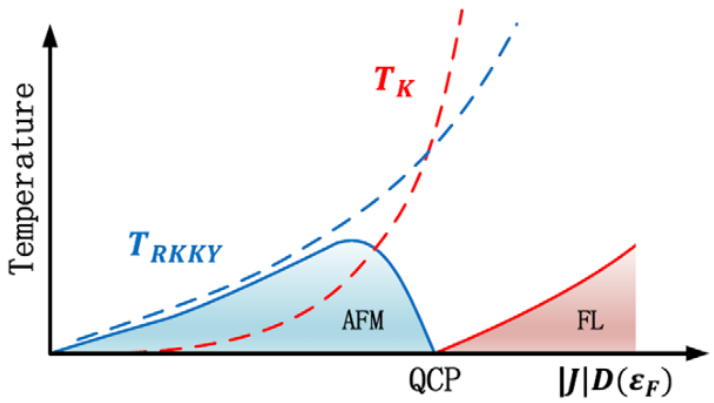

Figure 2.7: The Doniach phase diagram depicts the transition from a magnetically ordered state to a paramagnetic heavy Fermi liquid state, highlighting the passage through a quantum critical region that exists between these two phases as a control parameter $|J|D(\epsilon_F) = |JN(E_F)|$ is varied. Adapted from Ref. [22].

2.3 Weyl-Kondo semimetal (WKS)

Typically, investigations into topological phases have focused on weakly interacting systems. However, strongly correlated systems are particularly fascinating due to their complex phase diagrams and highly tunable ground states, especially in heavy fermion materials. Theoretical studies using the periodic Anderson model in noncentrosymmetric systems [23] and non-symmorphic Kondo lattices [19] with broken IS or TRS have shown that, when combined with strong electron correlations, Weyl nodal excitations can emerge with significantly reduced electron velocities. Furthermore, in the presence of strong corrolations, these Weyl nodes may be pinned to the Fermi energy [6].

An experimental example of this phenomenon is the Kondo-driven Weyl semimetal phase observed in $Ce_3Bi_4Pd_3$ [6]. The large magnitude of the spontaneous Hall effect has been interpreted as the result of the formation of Weyl nodes within the Kondo resonance, located in the immediate vicinity of the Fermi energy (Fig. 2.8b). Additionally, the theoretically calculated contribution to the electronic specific heat exhibits a cubic temperature dependence (Eq. 7) [23], which corresponds to the linear specific heat coefficient observed in $\Delta C/T$ as a function of T^2 (Fig. 2.8a).

$$C_v = \frac{7\pi^2}{30} k_B \left(\frac{k_B T}{\hbar v^*}\right)^3 \tag{7}$$

Here, k_B is the Boltzmann constant, $\hbar$ is the Planck constant, and v^* represents the

highly reduced quasiparticle velocity. The cubic temperature dependence of the electronic specific heat, $C_{el} \propto T^3$, directly indicates a linear electronic dispersion characteristic of Dirac and Weyl semimetals (see Fig. 2.8b).

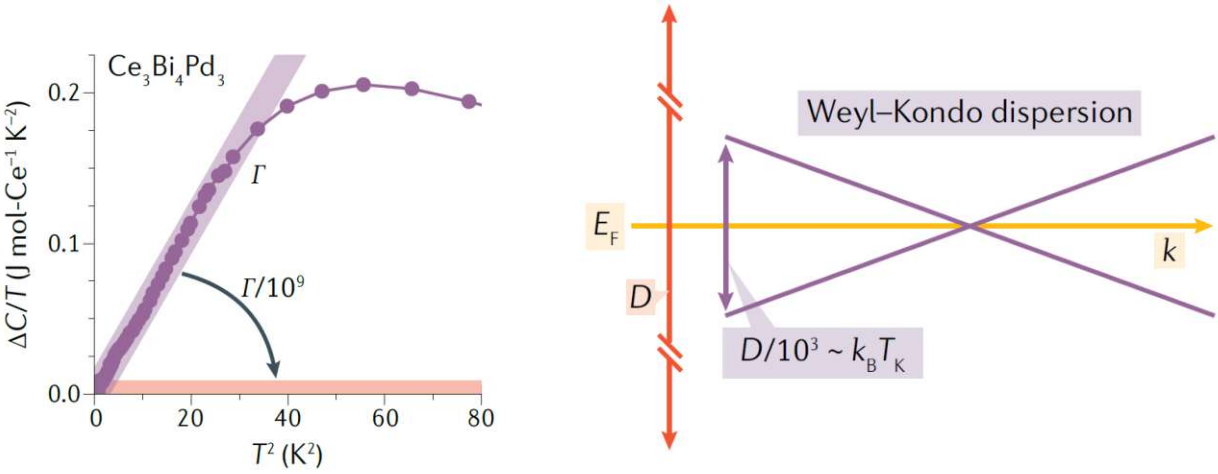

(a) (b)

Figure 2.8: a) Linear behaviour in T^2 of the electronic specifc heat over T at low temperatures. b) Linear electronic dispersion in momentum space near a Weyl point at the Fermi energy. Adapted from Ref. [1]

2.4 Chirality

A novel class of Weyl fermions has been identified in chiral systems. Chirality refers to a geometric object that cannot be superimposed on its mirror image. The simplest example of chirality is the human hand, as illustrated in Fig. 2.9a. Chirality manifests in various contexts, ranging from chiral particles in particle physics to chiral molecules in biology and medicine.

There are 65 space groups (SGs) that consist solely of symmetry operations of the first kind, thereby lacking inversion symmetry, mirror planes or any rotation-reflection axes [24]. The absence of improper symmetry operations (e.g., rotoinversion and rotoreflection) ensures that the crystal structure cannot be superimposed onto its mirror image, resulting in an enantiomeric pair with opposite chirality [25]. Furthermore, this class can be divided into 43 achiral SGs with chiral structures, which include the presence of the neutral 2_1,4_2 and 6_3 screw axes (see Fig. 2.9b), and 22 chiral SGs that contain at least one screw axis that is not the neutral screw axis. These include 11 enantiomeric pairs

[24].

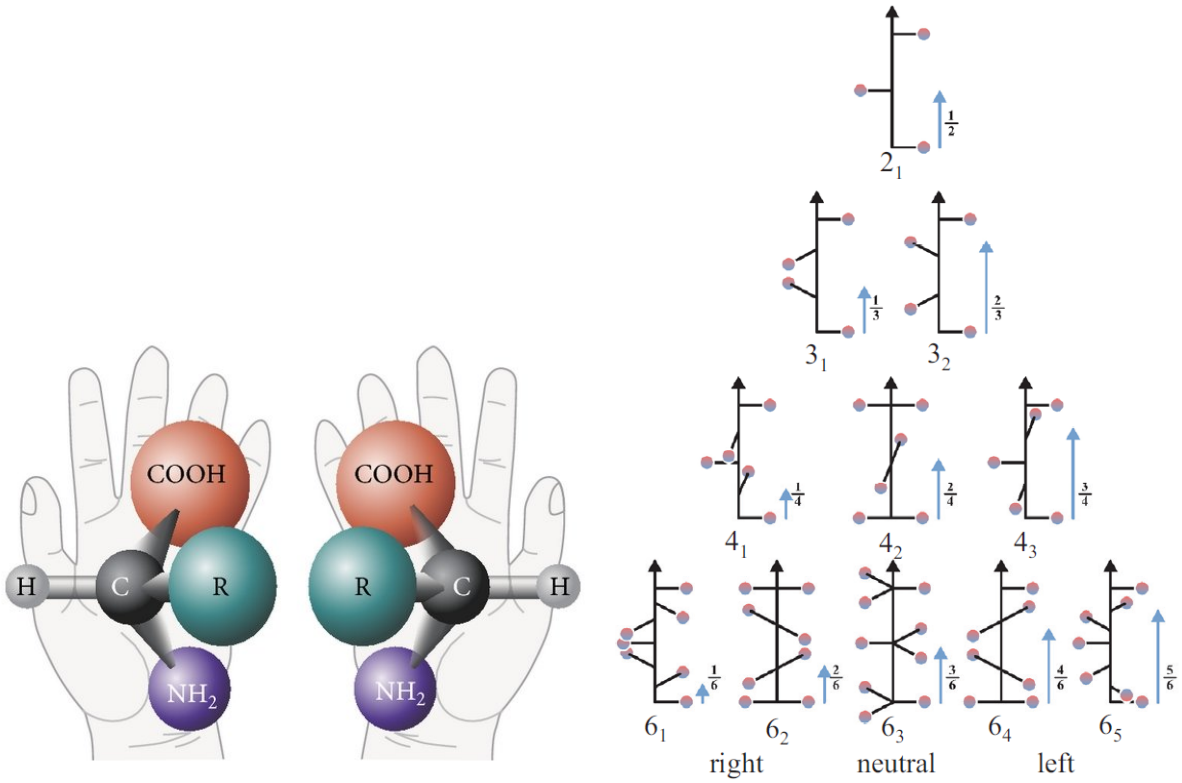

(a) (b)

Figure 2.9: a) Example for left and right handed chirality. Adapted from Ref. [26] b) Left, neutral, and right handed screw axis. Adapted from Ref. [24]

2.5 Kramers-Weyl semimetal (KWSM)

In the absence of specific crystal symmetries, as observed in chiral systems, a novel class of Weyl fermions known as Kramers-Weyl fermions has been identified [4]. In crystals that preserve TRS, Kramers theorem mandates the presence of doubly degenerate energy eigenstates at time-reversal invariant momentum points (TRIMs), given that the time-reversal symmetry operator $\mathcal{T}$ for half-integer spin systems satisfies $\mathcal{T}^2 = -1$. Spin-orbit coupling lifts degeneracies everywhere except at the high-symmetry TRIM points, where the Kramers degeneracy remains protected (see Fig. 2.10a) [4, 11]. The resulting Kramers-Weyl points are located at the center and the boundary of the Brillouin zone, thereby achieving maximal separation in momentum space. This configuration leads to the largest topological energy windows (see Fig. 2.10b) and facilitates the formation of

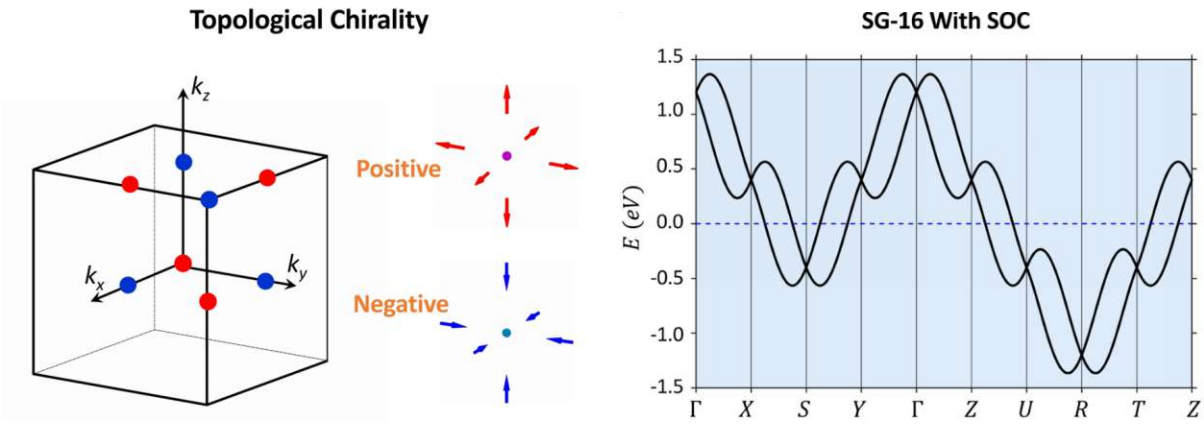

(a) (b)

Figure 2.10: a) Illustration of chiral fermions hosted at TRIMs in the Brillouin zone in all non-magnetic chiral crystals with SOC. b) The influence of SOC in Kramers-Weyl semimetals using SG 16 as an example. SOC splits the bands except at TRIMs, as deduced from Kramers theorem. Adapted from Ref. [4]

the longest possible Fermi arcs on the surface, as observed in the chiral Kramers-Weyl semimetal RhSi [10].

Moreover, they can give rise to monopole-like electron spin textures [27], chiral magnetic effects, and the quantized circular photogalvanic effect (CPGE) [4]. In the CPGE, circularly polarized light generates a measurable electric current within the material. When illuminated by this light, an asymmetry in the absorption of left- versus right-handed circular polarization occurs, leading to an imbalance in the population of charge carriers. This imbalance results in a current that flows perpendicular to both the direction of light propagation and its polarization [28].

Additionally, they may be utilized in the development of spin-torque devices [29]. In systems lacking inversion symmetry, Kramers-Weyl points can also influence superconducting pairing mechanisms and magnetic exchange interactions [30].

In symmorphic chiral SGs, all Kramers degeneracies exhibit Kramers-Weyl nodes situated at time-reversal invariant momenta. Conversely, in non-symmorphic SG, nodal planes may emerge alongside isolated Weyl nodes when specific screw rotation symmetries interact with time-reversal symmetry. To preserve a two-fold degeneracy for a given crystal symmetry $\mathcal{S}$, it is necessary that $\mathcal{T} \times \mathcal{S}$ returns a momentum point k to itself and satisfies the condition $\mathcal{T}^2 = -1$ for that particular value of k.

It has been demonstrated that nodal planes can be enforced by screw rotation symmetries associated with: two-fold rotations combined with a 1/2 lattice translation (2_1), four-fold rotations accompanied by a 1/4 translation (4_1) and six-fold rotations with either a 1/6 translation (6_1) or a 1/2 translation (6_3) [4]. In particular, a two-fold rotation axis characterized by $\mathcal{T} \times 2_1$ results in the formation of a nodal plane at $k_i = \pi$.

2.6 Kramers Weyl Kondo semimetal

So far, the investigation of Kramers Weyl fermions has primarily focused on non-interacting systems and those with weak electronic correlations. However, it is anticipated that strong correlations, in combination with spin-orbit interactions and reduced SG symmetries, may give rise to a rich variety of topological states of matter, analogous to Weyl Kondo semimetals [1]. The effects and potential properties of such material candidates remain open for exploration and could lead to new discoveries, although a well-defined theoretical framework has yet to be established.

In this work, we will investigate a candidate identified as a Kramers Weyl Kondo semimetal, characterized by its chiral structure, strong spin-orbit coupling, and indications of significant electronic correlations. It may be possible that within the Kondo coupling regime, the coherence of the electrons may tune the Kramers Weyl fermions to the Fermi level. Furthermore, multifold fermions are expected to emerge, which are associated with intriguing phenomena such as the chiral anomaly and the CPGE [4, 28].

2.7 Hall effect

Hall measurements have become a powerful tool to investigate strongly correlated systems as well as topological materials. Heavy fermion systems, known for their large effective masses and complex interactions, display unique transport phenomena that can be investigated using Hall effect measurements. These measurements often reveal anomalous behaviour related to skew scattering and the interaction between localized f-electrons and conduction electrons [31]. For topological materials, Hall measurements have emerged as a crucial technique for detecting and quantifying Berry curvature effects. The singularities of the Berry curvature field, an intrinsic property of electronic wave functions in momentum space, can act as magnetic monopoles and lead to unconventional transport

phenomena such as the anomalous Hall effect and the non-linear Hall effect [6, 32, 33].

In 1879, Edwin H. Hall conducted an experiment [34] in which he passed a current through a gold leaf while applying an external magnetic field perpendicular to the current direction. Due to the Lorentz force $\overrightarrow{F_L} = q(\vec{v} \times \vec{B})$ acting on the moving charge carriers, an electric field E_y is generated that is perpendicular to both the magnetic field B and applied current I. This results in a transverse voltage, known as the Hall voltage V_H, which balances the Lorentz force and establishes a steady state, with $V_H \propto B \cdot I$.

Consider a rectangular conductor with width b and thickness d (Fig. 2.11). A current is applied in I_x with charge carriers q, density n flowing with velocity v_x. Furthermore an external magnetic field is applied in B_z. The resulting transverse Hall voltage is given by $V_{xy} = E_y/b$ and within the free electron model [35]:

$$V_{xy} = \frac{1}{nq}\frac{I_x}{d}B_z = R_H\frac{I_x}{d}B_z \tag{8}$$

$R_H = 1/nq$ is called the Hall voltage and provides information about the type and the concentrtion of charge carriers in the conductor (electrons, holes, ions).

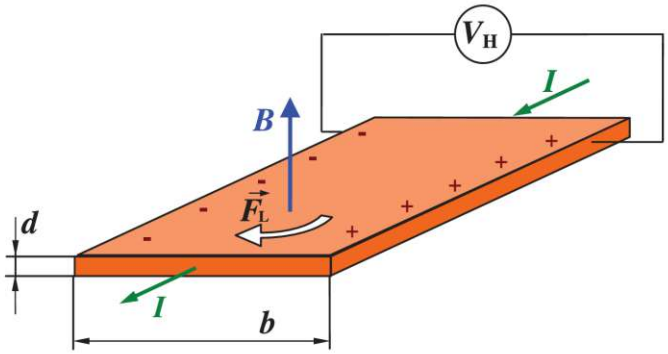

Figure 2.11: Schematic setup for a Hall measurement. Adapted from Ref. [35].

2.7.1 Anomalous Hall effect

The anomalous Hall effect (AHE) occurs in materials that exhibit broken time-reversal symmetry, which is commonly found in ferromagnets and topological materials. Unlike the ordinary Hall effect, the anomalous Hall effect is influenced not only by the Lorentz force but is fundamentally a quantum phenomenon arising from the coherent mixing of quantum states due to external electric fields and disordered potentials [36]. As a result, it

often exhibits a non-linear relationship between the Hall voltage and external parameters such as magnetic field strength or current density.

Research into the anomalous Hall effect began in the 19th century and has historically been complex and not entirely understood [36]. Currently, three distinct contributions to this effect have been identified. However, the overall picture remains incomplete, with several open questions still to be addressed. These contributions include the intrinsic contribution related to Berry curvature, as well as two extrinsic contributions known as skew scattering and side-jump effects [36].

In 1932, Pugh and Lippert [36] formulated an empirical expression for ferromagnetic materials:

$$\rho_{xy}(B) = R_O B_z + R_S M_z(B) = \rho_{xy,O} + \rho_{xy,A} \tag{9}$$

The transverse resistivity ρ_{xy} is governed by a linear component originating from the ordinary Hall effect, which depends on the external magnetic flux H_z and a constant R_O, arising from the Lorentz force. The second term on the right-hand side of Eq. 9 represents a characteristic contribution from magnetic materials, known as the AHE.

In single ferromagnetic domains, even in the absence of an external field, a net internal spontaneous magnetization generates a Hall signal. This phenomenon is referred to as the spontaneous Hall effect and depends on the magnetization M_z and a constant R_S [37].

The first theories for the origin of the anomalous contribution were introduced by Karplus and Luttinger in 1954 [38]. They considered an intrinsic contribution due to SOC in ferromagnetic materials. The spin-orbit interaction (SOI) of polarized conduction electrons in ferromagnetic crystals creates spin-dependent energy levels that interact with the interband matrix elements of the applied electric potential energy. This interaction promotes interband transitions, resulting in a transverse current that is both perpendicular to and proportional to the direction of magnetization and the applied electric field [37]. The topological nature of the intrinsic contribution, along with the concept of Berry curvature, came into prominence in 2002 [39].

When a quantum system undergoes adiabatic changes during a cyclic evolution from an initial state back to the same final state in the presence of SOC, the electron wave functions acquire a geometric phase known as the Berry phase, which arises from the trajectory in parameter space [40]. This results in a non-trivial contribution from the

Berry curvature. In Weyl semimetals, the existence of Weyl points leads to a non-zero Berry curvature that behaves like a magnetic field in momentum space, contributing to a transverse current when an electric field is applied. The transverse Hall conductivity is then given by [41]

$$\sigma_{xy}^{AH,int} = \frac{e^2}{\hbar} \int \frac{d\vec{k}}{(2\pi)^3} f(\epsilon(\vec{k}))\Omega_z(\vec{k}) \tag{10}$$

where $f(\epsilon(\vec{k}))$ presents the Fermi-Dirac distribution function for the energy eigenstates $\epsilon(\vec{k})$. Moreover, the equation of motion for a charged particle can be adjusted to incorporate an anomalous velocity term. This modification demonstrates that charged particles in a non-zero Berry curvature field behave analogously to how charged particles experience a Lorentz force in a magnetic field [41]:

$$\vec{v}_{Anomalous} = -\frac{e}{\hbar}\vec{E} \times \vec{\Omega}(\vec{k}) \tag{11}$$

Two additional extrinsic contributions to the AHE were proposed in 1958 by Smit, known as skew scattering, and in 1970 by Berger, referred to as the side jump mechanism [36]. Therefore, the anomalous Hall conductivity σ_{AH} consists of three terms:

$$\sigma_{AH} = \sigma_{AH}^{int} + \sigma_{AH}^{sk} + \sigma_{AH}^{sj} \tag{12}$$

where σ_{AH}^{int} is the intrinsic Berry curvature term, σ_{AH}^{sk} the extrinsic skew scattering and σ_{AH}^{sj} the extrinsic side jump term.

Skew scattering occurs when charge carriers are deflected by non-magnetic impurities or defects within the crystal. These carriers are preferentially scattered in one direction based on their momentum and spin orientation, resulting in a net transverse current when an electric field is applied [36]. This asymmetry can also arise from magnetic impurities that enhance one spin state. In 1958, Smit proposed that the anomalous Hall conductivity σ_{AH}^{sk} is influenced by the scattering rate and typically scales quadratically with the longitudinal conductivity $\sigma_{xy}^{AH} \propto \sigma_{xx}^2$ [32].

The side-jump effect occurs when an electron experiences a spin–orbit-coupled scattering event, resulting in a transverse displacement Δy. In 1970, Berger demonstrated that this mechanism contributes to the anomalous Hall resistivity with the relation $\rho_{xy}^{AH} \propto \rho_{xx}^2$ to the anomalous Hall resistivity [37].

2.8 Single crystal growth

The investigation of single crystals is of significant interest, as crystals can provide more accurate and reliable measurements of physical properties. This enhanced precision arises from reduced defects and impurities in single crystals compared to polycrystalline materials. Furthermore, studying the crystalline anisotropy inherent in single crystals is essential for understanding fundamental phenomena and the physical properties that are influenced by their underlying structure. Various crystal growth techniques are employed across a wide spectrum of applications, ranging from industrial uses to fundamental researches. The selection of an appropriate technique depends on the specific material and the desired quality of the resulting crystal. This study specifically focuses on the growth of single crystals from the melt using the floating zone method. The information provided in the following subsections is mainly retrieved from reference [42].

2.8.1 Principle of crystal growth from the melt

The growth of single crystals from the melt involves a complex interplay between thermodynamic stability and processes kinetics. Initially, a solid material is heated to achieve a molten state. Subsequently, this liquid is cooled to a critical supersaturation level, which initiates the nucleation process and facilitates further crystal growth.

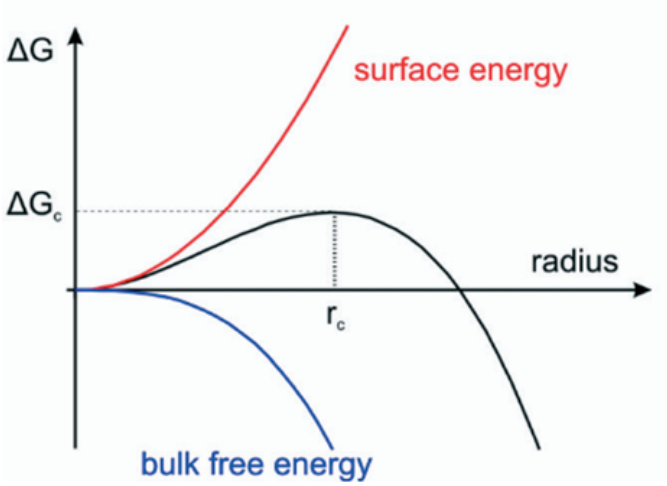

Figure 2.12: Gibbs free energy as a function of the nucleation radius on the left handside. The radius r_c defines the fist stable particles.

The cooling of a molten liquid results in the formation of a supercooled melt, which

provides the necessary conditions for nucleation processes to occur. The change in Gibbs free energy ΔG determines the thermodynamically favourability to form small clusters of atoms (a solid phase in the liquid). This energy is a sum of the competing volumetric contribution ΔG_V which favours nucleation by promoting the formation of a new phase, and the surface contribution ΔG_S, which opposes nucleation due to increased surface area.

$$\Delta G = \Delta G_V + \Delta G_S \tag{13}$$

In this resulting nucleation barrier a critical nucleus size, known as the critical radius r_c (Fig. 2.12), exists at which the nucleus becomes stable enough to grow rather than dissolve back into the melt. The rate of nucleation as well as the rate of growth, is controlled by the undercooling ΔT. A larger ΔT increases supercooling levels, leading to a higher nucleation rate but resulting in smaller crystals with potentially more defects. In contrast, a smaller ΔT favours fewer nucleation events, allowing existing nuclei to grow larger and more uniformly. This promotes better atomic arrangement within the crystal lattice, reducing the likelihood of dislocations and vacancies, which are detrimental to the crystal quality.

2.8.2 Optical floating zone technique

The floating zone crystal growth technique is renowned for its capacity to facilitate the production of high-purity single crystals. The advantage of this method is that no crucible is used, which effectively reduces the impact of contamination on the crystal. A typical setup consists of ellipsoidal or parabolic mirrors used to heat a molten zone of a vertical crystalline rod with one or more lamps. The growth configuration includes a feed crystal positioned at the top, a molten zone in the center, and a growing crystal at the bottom (Fig. 2.13a). The rod is gradually lifted as it rotates in a fixed position heater. In certain cases, the use of a seed crystal (single or polycrystalline) may be beneficial, particularly when the free energy of the nucleation barrier is excessively high. Upon contact between the seed crystal and the liquid, a monocrystalline structure grows on the seed crystal, adhering to its orientation and structure.

The liquid zone in this crucible free method is stabilized by the surface tension whereas the maximal length L_{max} is limited by the gravitational field g of the earth,

$$L_{max} = K \cdot \sqrt{\gamma/\rho g} \tag{14}$$

where ρ is the density of the liquid melt, γ the surface tension and K a factor depending on the meniscus angle, which defines the angle of the tangent between the liquid and the solid surface at their point of contact.

An optimal cylindrical form of the melt can only be reached in a microgravitional environment, whereas under terrestrial conditions the shape is controlled by gravity, as shown in Fig. 2.13b.

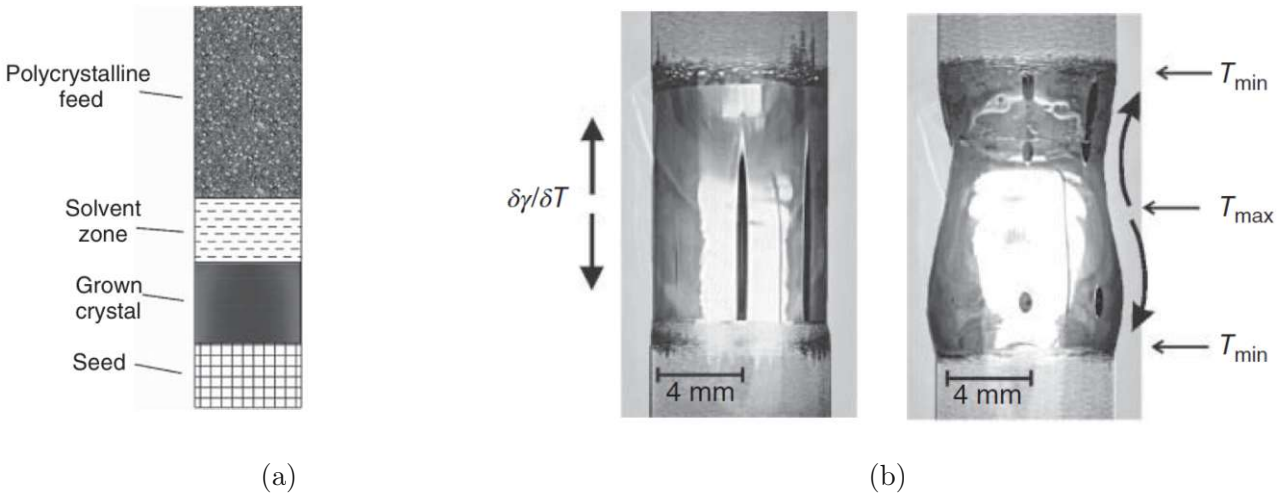

(a) (b)

Figure 2.13: a) Typical growth configuration in the optical floating zone furnace. b) Molten zone in a microgravitational environment features a cylindrical form and a bottle shape under terrestrial conditions. Adapted from Ref. [42].

This technique is also often used to purify crystals as the impurities tend to be concentrated in the melt. The impurity atoms with different electronic structures and sizes cause strain in the lattice and less favourable chemical bondings that increase the overall energy in the system. Furthermore, impurities contribute more to the overall entropy by remaining in the more disordered liquid state. This trend is evident in the segregation coefficient $k = C_S/C_L$, where C_S represents the impurity concentration in the solid crystal and C_L denotes the impurity concentration in the liquid. Typically, this coefficient is less than 1.

In the case of an incongruently melting compound, a solvent is used in the travelling solvent method [43].

3 Experimental background and methods

This section provides an overview of the techniques, apparatus, and measurement devices used for the growth of CeIrSi single crystal as well as the investigation of physical properties under extreme conditions, including electric transport, specific heat and magnetic properties at temperatures down to 2 K and high magnetic fields. The first section addresses the description of the investigation techniques employed, including Scanning Electron Microscopy (SEM), X-ray Diffraction (XRD), and Laue diffraction. This is followed by an explanation of the sample preparation and the process of single crystal growth using an optical mirror furnace. The focus then shifts to the equipment and techniques used to measure the physical properties and, finally, the procedure for Hall measurements.

3.1 Analytical investigation techniques

At first, a short introduction to the investigation techniques used to determine crystal structure, phase composition and chemical composition. This includes X-ray powder Diffraction (XRD), Scanning Electron Microscopy (SEM) and energy dispersive X-ray analysis (EDX) as well as Laue diffraction.

3.1.1 X-ray powder diffraction

X-ray powder diffraction (XRD) uses monochromatic X-rays to analyze the crystal structure of a material, providing insights into unit cell dimensions, atomic arrangement, and the crystalline phases present in the sample. As X-rays penetrate the material, they are scattered by atoms in various layers, which are identified by their Miller indices hkl (see Fig. 3.1). The constructive interference of the scattered light can be described using the incident wavelength λ, the interplanar spacing d_{hkl} of the atomic layers and the Bragg angle θ

$$n\lambda = 2d_{hkl} \cdot \sin\theta \tag{15}$$

where n presents the diffraction order [44].

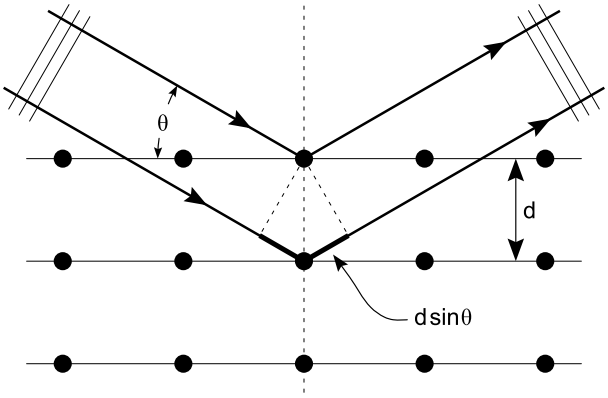

Figure 3.1: Reflection of X-rays on a set of crystallographic planes [45]

In this thesis, powdered samples were placed onto a single crystal silicon zero diffraction plate and analyzed using the multi-purpose diffractometer AERIS from Malvern Panalytical. The well-known Rietveld refinement method was employed to refine the crystal structure and extract the structural parameters.

3.1.2 Scanning electron microscopy & Energy dispersive X-ray analysis

Scanning electron microscopy (SEM) and energy dispersive X-ray spectroscopy (EDX) is used for imaging at the micrometer scale and the local elemental analysis of the sample's microstructure. Therefore, a beam of high-energy electrons ($\approx 30\,\mathrm{V_e}$) is directed onto the surface, generating various signals, including backscattered electrons (BSE), secondary electrons (SE), and element specific X-rays [46]. SE and BSE are used for the topological characterization and imaging of the sample surface. The characteristic X-rays are emitted as inner-shell electrons are ejected by the incident beam and outer-shell electrons fill the vacancies. The analyses are performed as calibration free measurements with uncertainties of ±1At.%.

3.1.3 Laue diffraction

Laue diffraction is a well-established technique for evaluation of the quality and determining the orientation of single crystals. Polychromatic X-rays are focused on a stationary

single crystal and reflected by the atomic plane arrays according to the Bragg equation (15). Since d and θ are fixed, constructive interference of the X-rays occurs for specific incident wavelengths λ and diffraction orders n, resulting in spots on the detector that correspond to particular sets of crystallographic planes (hkl). These spots are arranged in ellipses, forming a characteristic Laue pattern that reflects the underlying crystal structure.

For further reading and deeper understanding, see reference [47].

3.2 Optical floating zone technique

The crystal growth is performed using the travelling heater method in a FZ-T-1000-H-VI-VPM-PC mirror furnace from Crystal Systems Corporation, equipped with four 1500 W lamps. The schematic setup is shown in Fig. 3.2a. These lamps are positioned within four ellipsoidal mirrors, ensuring optical heating with a focal spot centered on the sample. An overpressure argon atmosphere of 1.5 bar inside a quartz tube prevents oxidation and unwanted diffusion processes.

Two polycrystalline rods with a stoichiometric composition and a diameter of 5 mm were prepared to serve as seed and feed crystals. Additionally, a solvent is attached to the bottom of the feed rod.

The experimental setup is shown in Fig. A.1 in the Appendix.

3.3 Electric transport

Electric transport measurements conducted on monocrystalline rectangular samples of CeIrSi, included resistivity measurements for two different orientations, as well as field-dependent resistivity and Hall effect measurements in the crystallographic direction [100] up to 9 T. These measurements were performed using the four-point technique. Therefore, the samples were contacted via spot welding with gold wires of diameter $d = 25\,\mu m$. Two outer contacts, aligned in the longitudinal direction of the sample, served as the current supply, as shown in Fig. 3.3. The voltage drop V_{xx} across the sample, resulting from its internal resistivity, was measured using two separate inner contacts. The Hall voltage V_{xy}, associated with both spontaneous Hall effect and field-induced Hall effect,

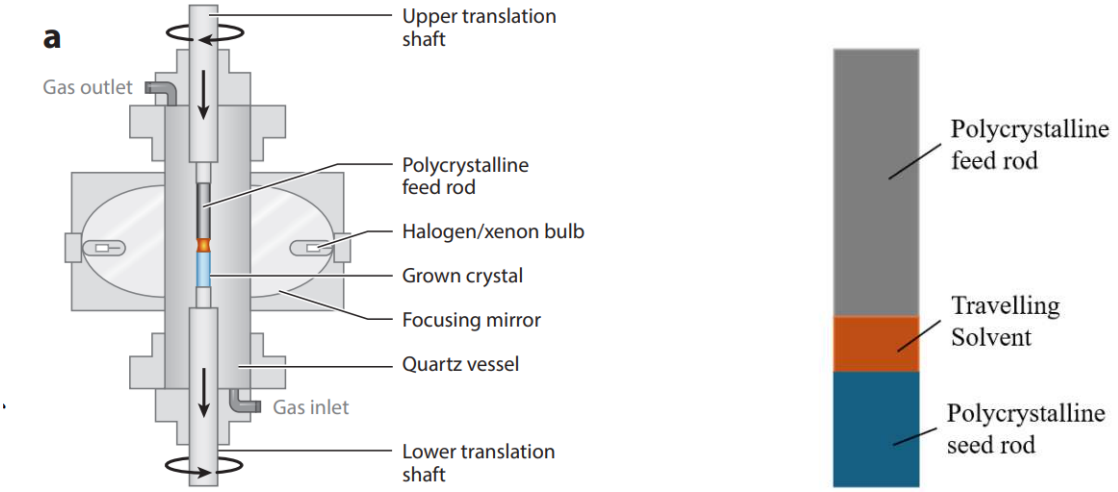

(a) (b)

Figure 3.2: a) Schematic setup of a mirror furnace with parabolic mirrors and optical heating. Adapted from Ref. [48]. b) Rod configuration in the mirror furnace with seed, feed rod in stoichiometric composition and a solvent in off-stoichiometric composition.

was measured using two contacts positioned transversely, perpendicular to the applied current. This configuration of separate contact pairs effectively eliminates contributions from contact resistance, which can exceed the actual intrinsic resistivity of the sample.

The Resistance can be calculated using Ohm's law:

$$R_{xi} = \frac{V_{xi}}{I_x} \quad \text{with} \quad i = x,y \tag{16}$$

Considering the samples geometry (thickness d, width b) and contact placement (length L_{xx}), the longitudinal resistivity ρ_{xx} is given by

$$\rho_{xx} = R_{xx}\frac{b \cdot d}{L_{xx}} \tag{17}$$

The transverse resistivity ρ_{xy}, on the other hand, is determined by the transverse resistance R_{xy} and the thickness d:

$$\rho_{xy} = R_{xy} \cdot d \tag{18}$$

Figure 3.3 shows the ideal setup with perfectly aligned contacts. However, in practice, contacting the small samples often results in misalignment, which can significantly affect measurements taken in a magnetic field. A well-established technique to address this

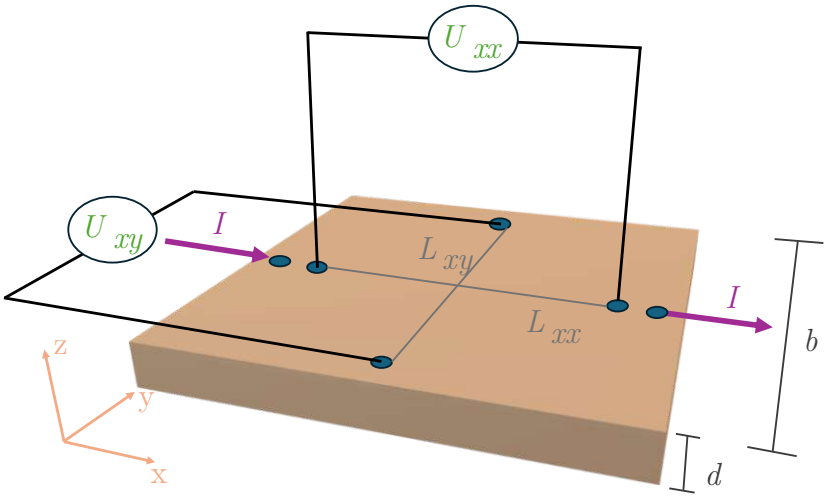

Figure 3.3: Experimental setup for electric transport measurments

issue involves measuring the Hall resistance in both positive and negative fields, followed by symmetrizing the R_{xx} component and antisymmetrizing the R_{xy} component.

$$R_{xx}^{S} = \frac{R_{xx}(B) + R_{xx}(-B)}{2} \tag{19}$$

$$R_{xy}^{A} = \frac{R_{xy}(B) - R_{xy}(-B)}{2} \tag{20}$$

The longitudinal resistance should be homogeneous and stable; therefore, antisymmetric contributions are expected to account for misalignment or other sources of instability. In contrast, the antisymmetrization of the Hall signal ensures that only the Hall effect is considered, eliminating any contributions from the longitudinal signal.

AC resistivity and field-dependent resistivity measurements from 300 K to 2 K has been performed by using the PPMS He^4 cryostat with a superconducting magnetic coil from Quantum design. The spot welded contacted sample has been glued on a sample holder with GE vanish. Magnetic fields were applied perpendicular to the current up to 9 T. Switching from positive to negative fields in the PPMS system has been realized with a horizontal rotator.

Hall measurements were performed using a VTI flow cryostat from Oxford Instruments. Similar to the Setup in the PPMS, the sample was glued onto a sample holder with GE varnish. Magnetic fields up to 15 T were applied perpendicular to the direction of the

current over a temperature range from 300 K to 1.85 K.

3.4 Heat capacity

Measuring the heat capacity of solids serves as a powerful tool for elucidating the magnetic, electronic, and lattice properties of materials. Particularly at low temperatures, it facilitates direct comparisons between experimental and theoretical predictions of certain energy levels. Additionally, heat capacity measurements facilitate the calculation of the systems entropy and can probe phase transitions when combined with other electrical transport measurements, such as resistivity [49, 50].

The total heat capacity for a metallic magnetic material includes electrons, phonons and magnons [2]:

$$C_p(T) = C_{el}(T) + C_{ph}(T) + C_m(T) \tag{21}$$

And in the absence of magnetic contributions:

$$C_p(T) = \gamma T + \beta T^3 \tag{22}$$

where the Sommerfeld coefficient γT, which is known to indicate strong electron correlations, accounts for electronic and βT^3 for phonon contributions to the total specific heat.

The PPMS employs the well-established thermal relaxation method to measure heat capacity $C_p = (dQ/dT)_p$ at constant pressure over a temperature range from 300 K to 2 K. In a typical setup, the sample is mounted using thermal grease onto a platform equipped with a heater and thermometer, as shown in Fig. 3.4.

The sample is heated for a limited time dT/dt, after which the exponential temperature decay during cooling is monitored. This can be described by a heat balance equation with the total heat capacity C_{total}, a thermal conductance parameter K_w, the bath temperature T_{bath} and the supplied heat power $P(t)$ [49]:

$$C_{total}\frac{dT}{dt} = -K \cdot (T - T_{bath}) + P(t) \tag{23}$$

The solution to this differential equation is given by:

$$T(t) = T_{bath} + \Delta T \exp\left(-\frac{t}{\tau}\right) \tag{24}$$

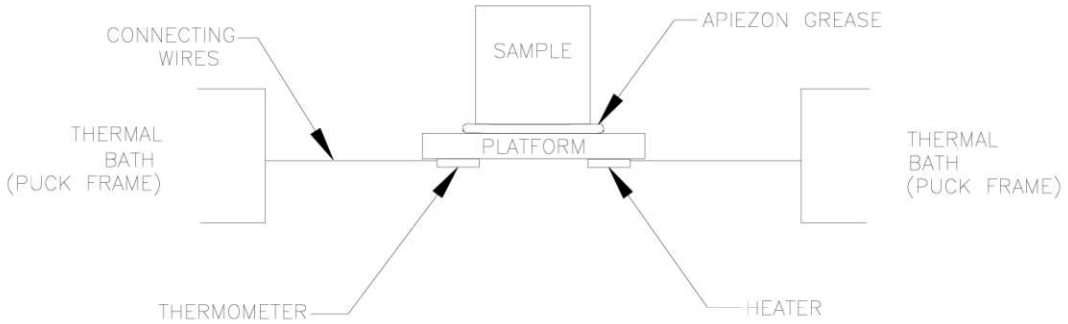

Figure 3.4: Experimental setup for measuring the heat capacity in PPMS. Adapted from Ref. [49].

with the thermal relaxation time $\tau = C_{total}/K$.

The heat capacity of the sample can be determined by conducting an addenda measurement of the platform without the sample and subtracting it from the total heat capacity:

$$C_{sample} = C_{total} - C_{platform} \tag{25}$$

3.5 Vibrating sample magnetometer

The PPMS vibrating sample magnetometer (VSM) is used to measure the magnetic properties of samples within a temperature range from 300 K to 2 K and under magnetic fields of up to 6 T. The VSM operates on an induction-based principle, measuring the magnetic moment of the sample via a pickup coil while the sample vibrates perpendicular to a uniform magnetic field, as shown in Fig. 3.5. For a magnetic sample, the magnetic moments align with the external magnetic field B. As the sample oscillates vertically, a changing magnetic flux $d\Phi/dt$ induces a voltage V_{coil} in the pickup coils, which is proportional to the sample's magnetization. The sample is affixed to a quartz holder and driven sinusoidally at a frequency of $f = 40$ Hz within the magnetic field. Consequently, the magnetic moment μ can be expressed as [51]:

$$\mu = \frac{V_{coil}}{2\pi f C A \cdot \sin(2\pi f t)} \tag{26}$$

where C is the coupling constant and A is the amplitude of the oscillation.

Finally, the molar magnetization M and the susceptibility χ can be determined using the mass of the sample m_{sample}, the molar weight M_w of CeIrSi $M_w(\mathrm{CeIrSi}) = 360.418\,\mathrm{g/mol}$

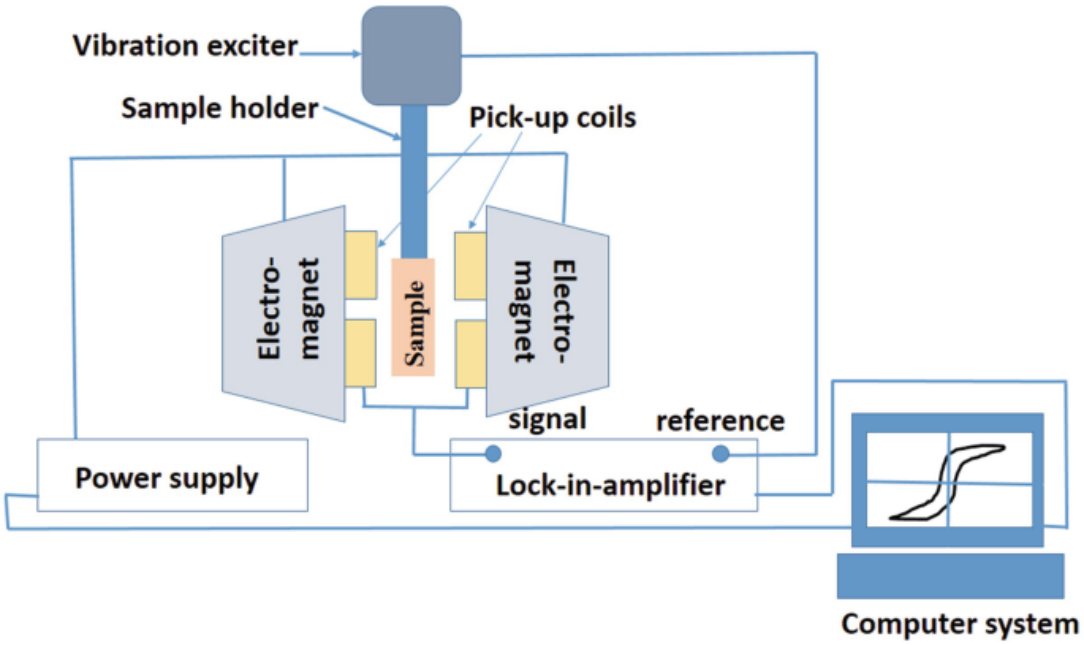

Figure 3.5: Schematic setup for a vibrating sample magnetometer. Adapted from Ref. [52].

and the magnetic field strength H:

$$M = \frac{\mu \cdot M_w}{m_{sample}}; \qquad \chi = \frac{M}{H};$$

4 State of the Art - CeIrSi

4.1 Structural investigations

Previous investigations by *F.Kneidinger et al.* [12] on polycrystalline samples of CeIrSi, as well as studies by *B Heying et al.* [53] of single crystal X-ray diffraction revealed the cubic chiral space group 198 ($P2_13$) with a lattice constant $a = 629.51(1)$ pm (629.15(2) pm respectively). Nearest Ce neighbours crystallize within a trillium type structure (see inset of Fig. 4.1). Trillium lattice arrangements are known to host complex magnetic interactions due to their geometrical frustration. Powder X-ray diffraction of polycrystalline samples by *F.Kneidinger et al.* revealed the impurity phases $CeSi_{2-x}$ and $CeIr_2Si_2$.

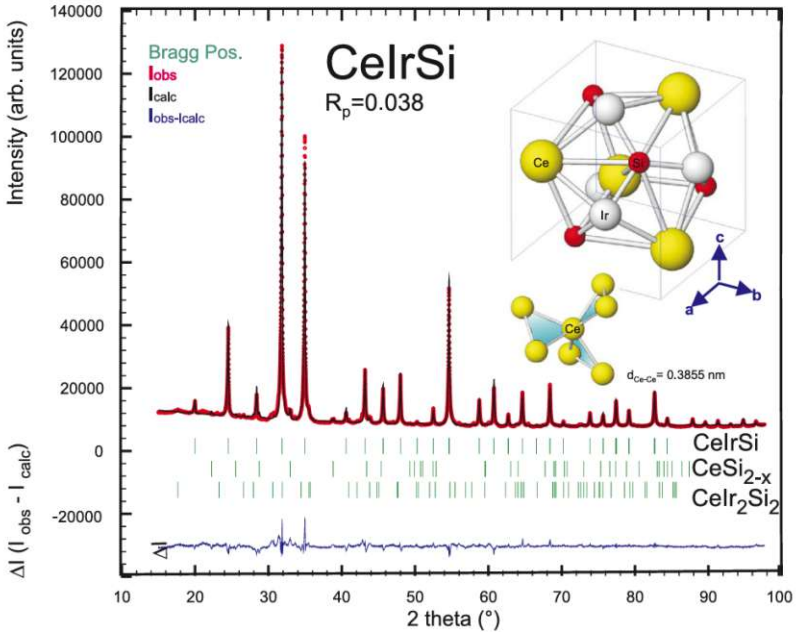

Figure 4.1: Rietveld refinement for polycrystalline samples of CeIrSi. Small amounts of impurities are visible in the spectra. The inset show the unit cell for CeIrSi as well as the trillium structure type for Ce. Adapted from Ref. [12]

4.2 Physical properties

F.Kneidinger et al. identified this material as a paramagnetic compound down to 0.3 K characterized by dominant antiferromagnetic interactions among the Ce^{3+} ions. Fer-

romagnetic contributions observed below the critical temperature $T_c = 11\,\mathrm{K}$ (see inset of Fig. 4.2) were attributed to foreign phases, specifically $CeSi_{2-x}$ (with $x = 0.2$) and $CeIr_2Si_2$. Additionally, spurious contributions at approximately $T \approx 6\,\mathrm{K}$ were linked to traces of oxide impurities [12].

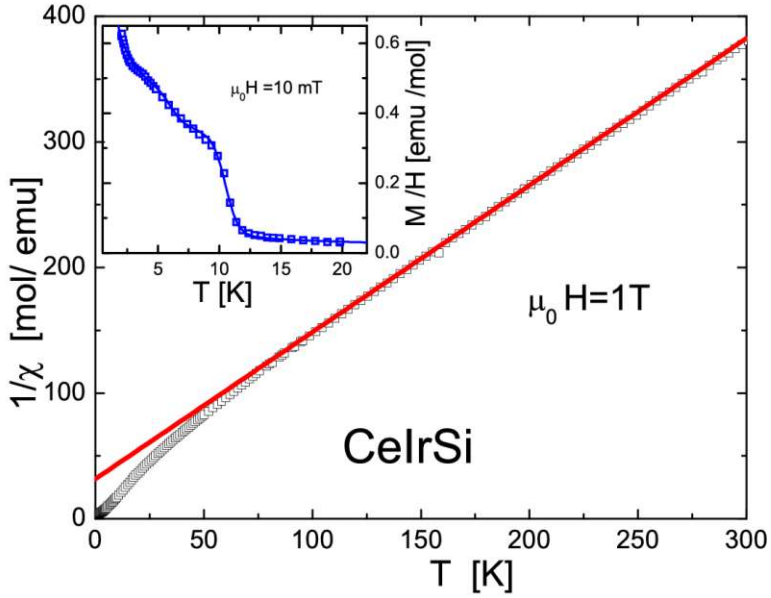

Figure 4.2: Inverse susceptibility of CeIrSi in an external field of 1 T. The inset shows ferromagnetic contributions below 11 K. Adapted from Ref. [12]

Magnetic anomalies observed at 1 K and 1.2 K were addressed to two magnetic phases (see Fig. 4.3).

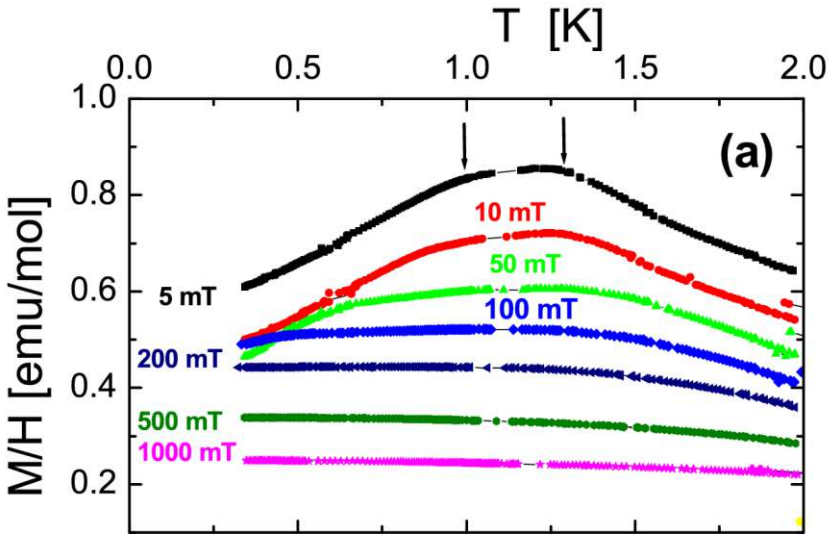

Figure 4.3: Low-temperature magnetization curves measured in relatively low magnetic fields reveal two distinct anomalies. Adapted from Ref. [12]

Electrical transport measurements reveal a semiconducting type behaviour as shown in Fig. 4.4. At low temperatures, the resistivity decreases under applied magnetic fields due to spin alignment along the field direction, which reduces spin-dependent scattering. In contrast, no significant field-induced effect is observed at temperatures above 60 K.

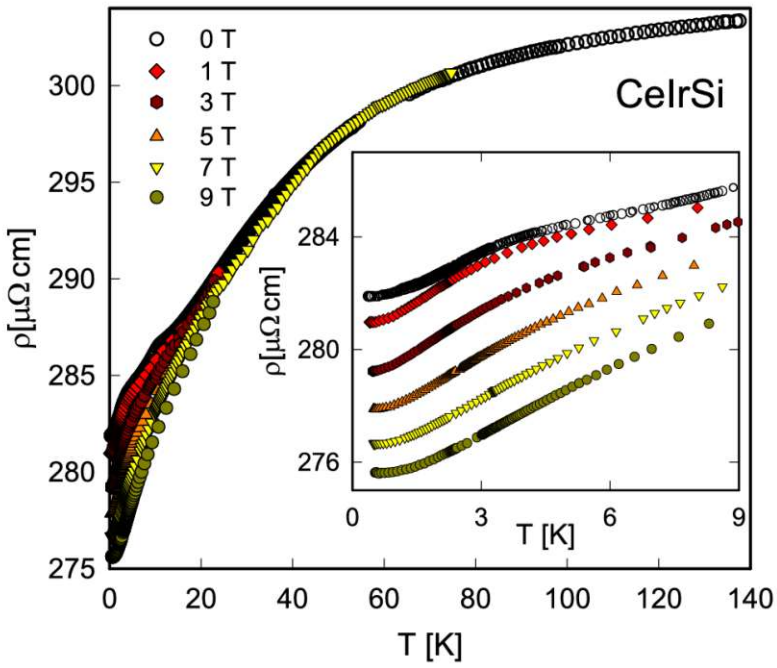

Figure 4.4: Temperature and field dependent electrical resistivity measurements. The inset shows the field dependencies below the critical temperature T_c. Adapted from Ref. [12]

5 Results

In the following section, the growth, structural characterization, and physical properties of CeIrSi are presented in detail. Beginning with the investigation of polycrystalline samples to evaluate phase formation and stability, the section progresses to the successful single crystal growth using the optical floating zone technique. The structural quality and composition are assessed through X-ray diffraction, SEM, and EDX. Subsequently, temperature- and field-dependent measurements of heat capacity, magnetization, electrical resistivity, field-dependent resistivity, and Hall effect are discussed. These results provide insight into the complex magnetic ordering and electronic correlations in this non-centrosymmetric compound and suggest the presence of multiple magnetic phases at low temperatures.

5.1 Polycrystalline CeIrSi

To achieve successful single crystal growth of CeIrSi in the optical floating zone setup, it is essential to investigate the phase relation in the ternary Ce-Ir-Si system and determine the phase diagram. The previous investigation of the ternary alloy at an isothermal section at 950° [13] serves as a starting reference, as shown in Fig. 5.1.

Polycrystalline samples were synthesized using high-purity elements in stoichiometric proportions. The elements were melted in a high-frequency furnace under an argon atmosphere to minimize oxidation. X-ray diffraction confirmed the presence of the desired phase CeIrSi. However, secondary phases $CeIr_2Si_2$ and $Ce_3Ir_2Si_2$ were also detected, comprising a not negligible fraction of approximately 40% (Fig. 5.2).

The secondary phases did not disappear after annealing the sample for 5 days at 950°.

SEM images of polished sample surface (Fig. 5.3) revealed the crystallization sequence during the cooling process

$$CeIr_2Si_2 \rightarrow \mathbf{CeIrSi} \rightarrow Ce_3Ir_2Si_2$$

suggesting an incongruently melting CeIrSi compound.

EDX measurements indicated a small deviation from the stoichiometric composition of

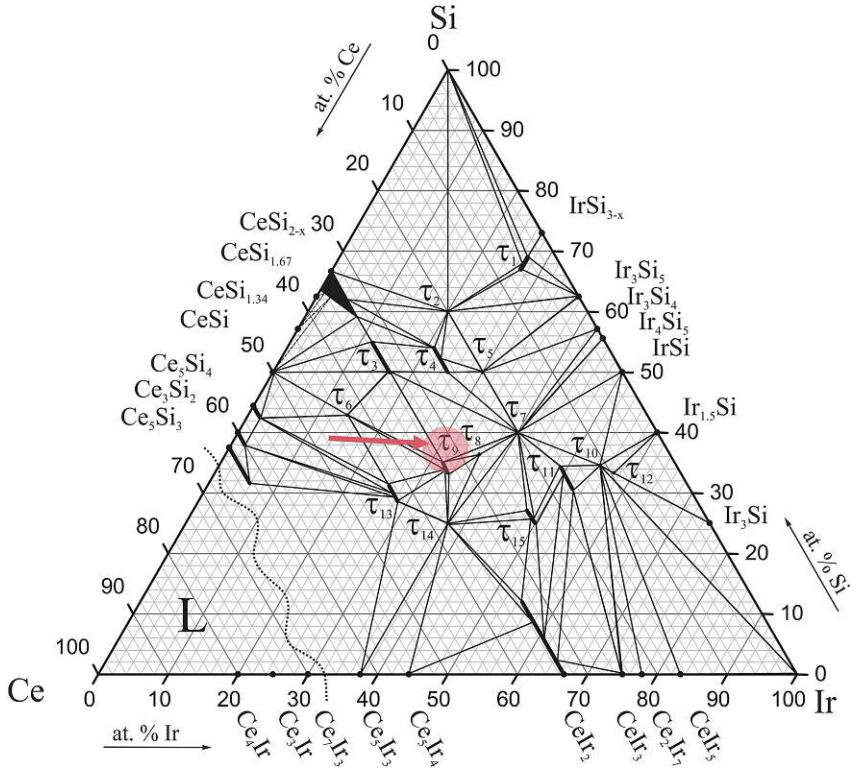

Figure 5.1: Ternary phase diagram for Ce-Ir-Si at an isothermal section of 950 °C [13]. The target compound CeIrSi is refereed to τ_9.

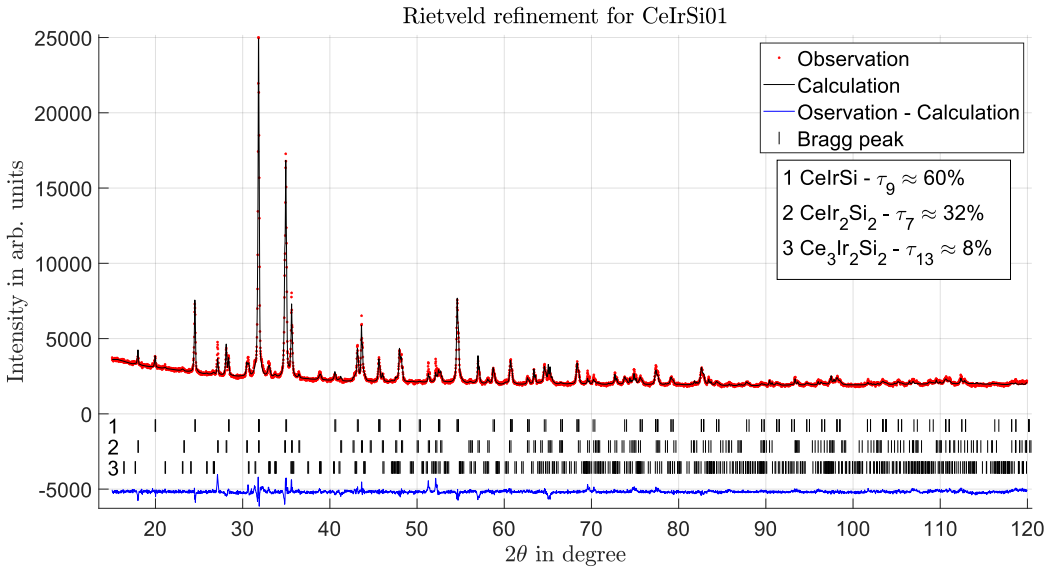

Figure 5.2: Rietveld refinement of powder XRD for as-cast sample CeIrSi01. Relative intensity as function of 2θ diffraction angle, calculated fit by Rietveld refinement shown as black curve, and difference illustrated as blue line. The position of the Bragg peaks is indicated by black strips underneath. The identified phases and their proportion are listed in the upper right corner.

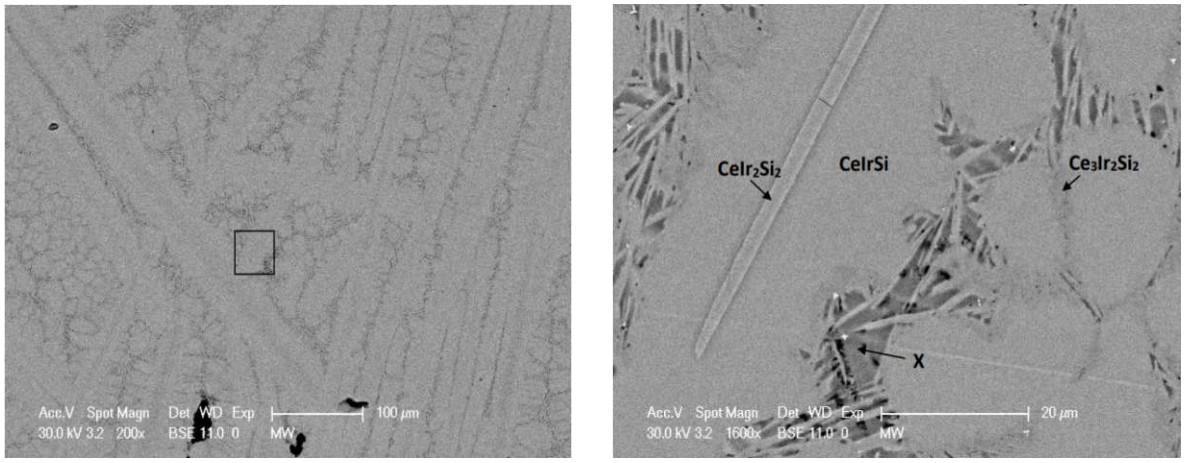

(a) (b)

Figure 5.3: a) SEM images for the polycrystalline sample CeIrSi01. b) Determined phases in the enlarged image of figure a).

the CeIrSi phase, showing higher Si ($\approx 36\%$) and lower Ir content ($\approx 32\%$) in the target phase. This may be explained by the substitution of Si in the Ir sublattice.

The assumption of an incongruent melting character, combined with the information on the crystallization sequence and the performed differential thermal analysis (DTA), provides an initial tentative phase diagram as shown in Fig. 5.4. It shows a primary crystallization field for CeIrSi extending from the stoichiometric composition toward higher Ce concentrations. A peritectic point is located at approximately35% Ce on the x-axis.

Based on this, the composition is adjusted from the initial 33.3% Ce to 37.5% Ce, which, according to the phase diagram, shifts the material away from the $CeIr_2Si_2$ phase field and promotes the formation of CeIrSi. This adjustment leads to a polycrystalline sample with an overall composition of approximately 75% CeIrSi.

Two different methods were employed for the single crystal growth: crystal growth using common fluxes and the floating zone technique. However, only the second has been successful and is therefore worth discussing in more detail.

5.2 Single crystal

For the single crystal growth of CeIrSi, the travelling solvent floating zone (TSFZ) method is necessary due to the incongruent melting of the compound. Incongruent melting limits

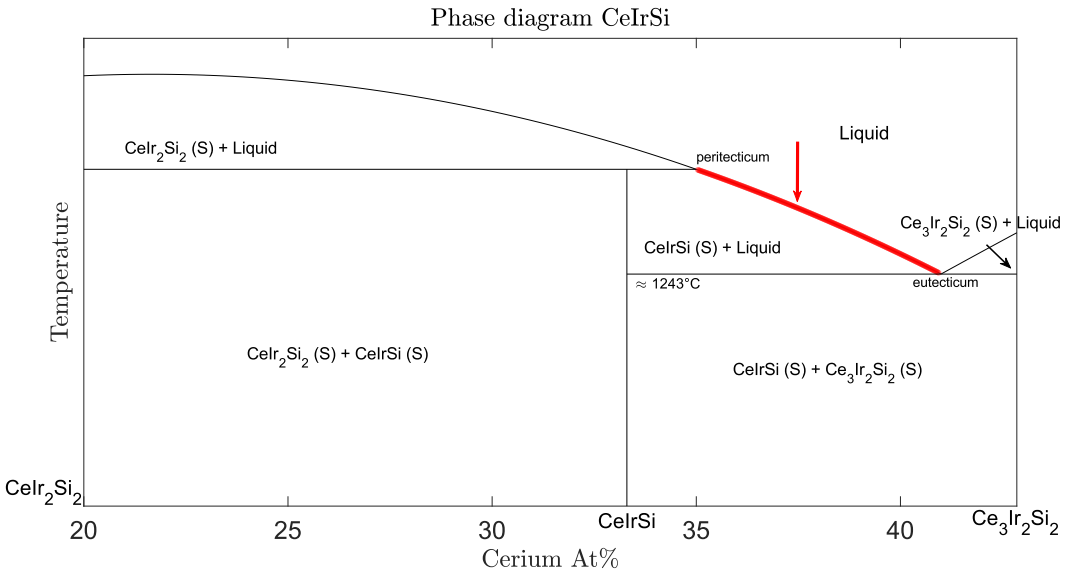

Figure 5.4: Schematic temperature-composition diagram for the ternary compound CeIrSi

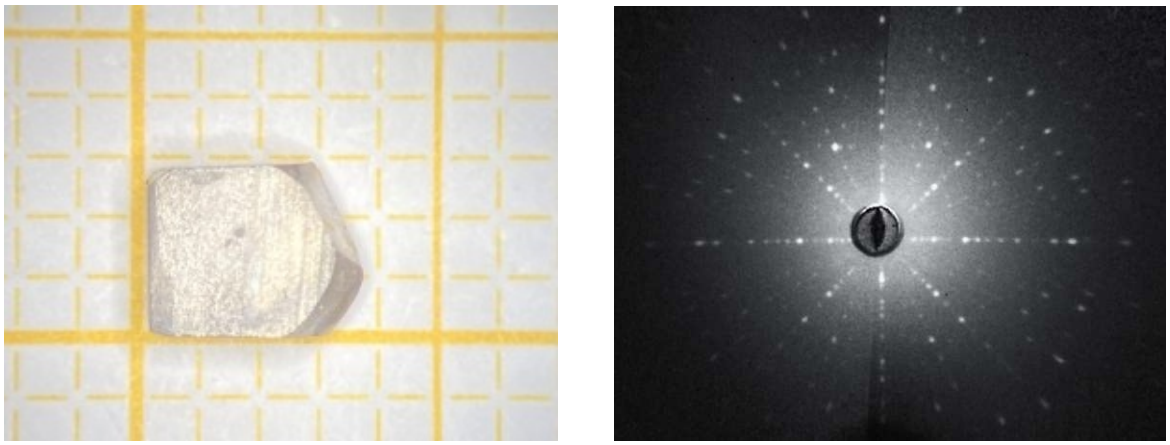

(a) (b)

Figure 5.5: a) Extracted single crystal of CeIrSi b) CeIrSi single crystal Laue pattern in the crystallographic direction [100].

the formation of the target phase to a specific region of the phase diagram, particularly within the primary crystallization field of CeIrSi, which extends from the peritectic to the eutectic point, as shown in Fig. 5.4. For this purpose, a solution with the previously optimised composition containing 37.5% Ce is used as a travelling solvent in the optical floating zone setup.

A crystalline rod with a length of 33 mm was successfully grown in the optical mirror furnace using a growth rate of 0.3 mm/h. SEM, EDX, and Laue diffraction analyses

confirmed the growth of monocrystalline CeIrSi. A single crystal from this batch, oriented along the (100) plane (see Fig. 5.5b), was cut into a piece measuring $3.5 \times 3 \times 2\,\text{mm}$ (l, w, h) (see Fig. 5.5a).

SEM and EDX analysis confirmed a high-purity single crystal of CeIrSi, free of impurities and close to the stoichiometric composition, as shown in Tab. 1.

Table 1: Composition of CeIrSi single crystal

Phase	Atom %		
	CeL	IrL	SiK
CeIrSi	33.41	33.30	33.30

The structural parameters of CeIrSi were determined by the Rietveld refinement from powder XRD (see Tab. 2 and Fig. 5.6). Calculations were performed using the *FullProf* software.

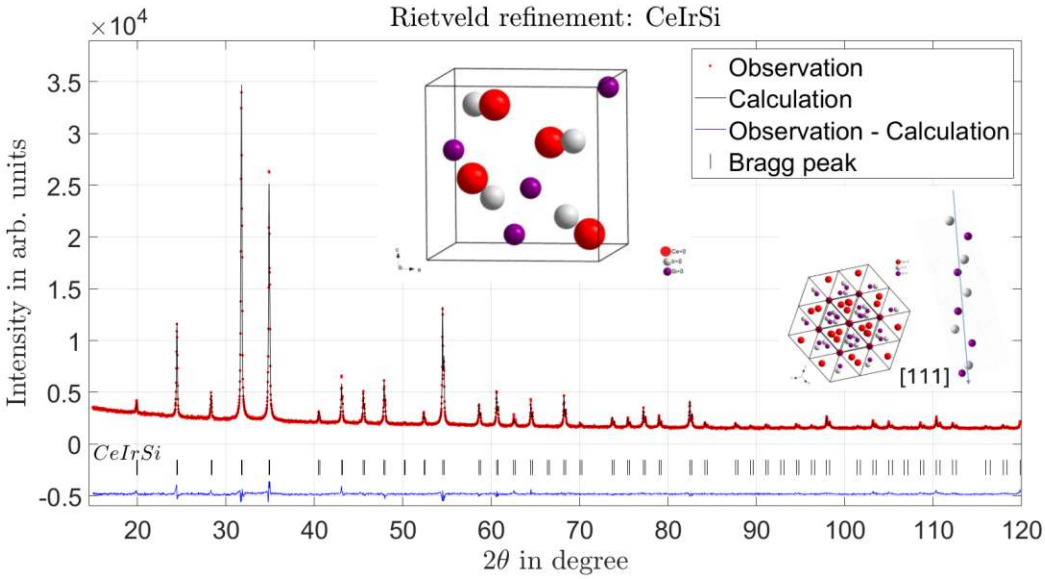

Figure 5.6: Rietveld refinement for powder XRD spectra of single crystal CeIrSi. Characteristic Bragg peaks are indicated by sharp lines underneath.

5.2.1 Sample declaration

The extracted single crystal was polished into a rectangular shape for physical property measurements, maintaining its orientation along the crystallographic (100) plane. This

Table 2: Structural parameter of CeIrSi determined from refined powder XRD data

Space Group	$P2_13$/ No.198
Pearson symbol	$cP12$
Formula weight (g/mol)	360.41
Lattice parameter $a = b = c$ (pm)	629.44(1)
Literature [12]	629.51(1)
Literature [53]	629.15(2)
Density (g/cm^3)	9.833
Wickoff position Ce, Ir, Si	$4a$
Atomic coordinates	$x = y = z$
Ce	0.3660(2)
Ir	0.0784(2)
Si	0.6573(7)

sample is hereafter referred to as CeIrSi-S1. For electrical transport measurements, gold wires were attached via spot welding, as illustrated in Fig. 5.7. Furthermore, a single crystal was prepared approximately along the crystallographic plane (110), called CeIrSi-S2 (see Fig. 5.8a), shown in Fig. 5.8b.

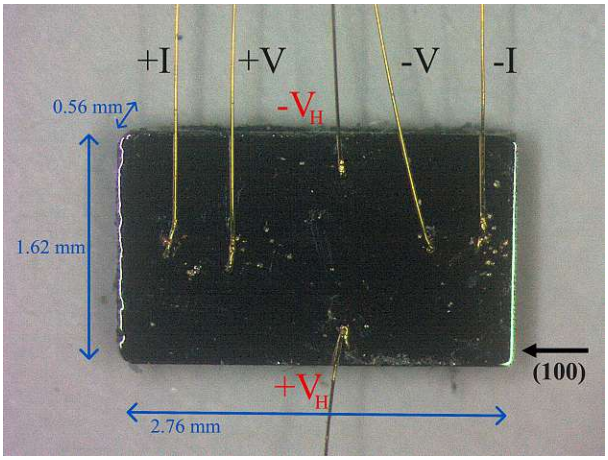

Figure 5.7: Single crystal sample CeIrSi-S1, oriented along the (100) plane, contacted with gold wires.

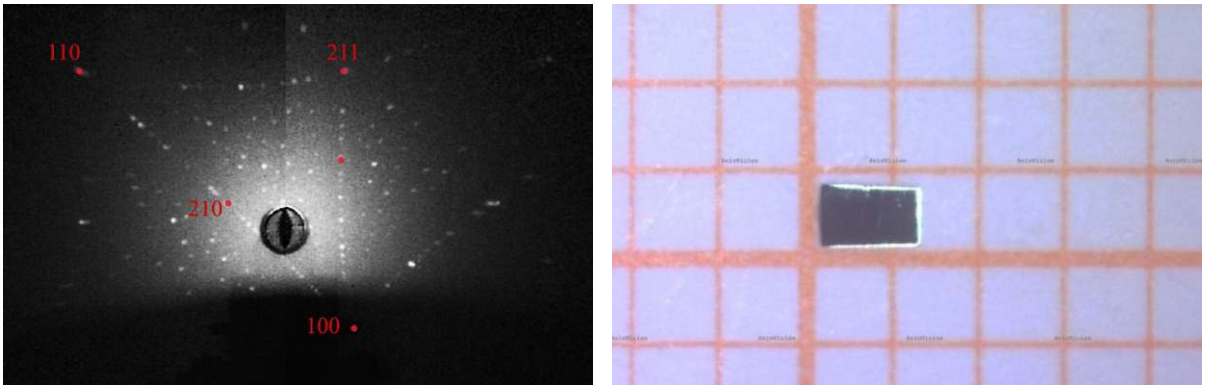

(a) (b)

Figure 5.8: a) Laue image for single crystal sample CeIrSi-S2, oriented approximately in [110]. b) Sample CeIrSi-S2 placed on a 1×1 mm square ruled paper.

5.3 Heat capacity

The heat capacity at constant pressure C_p for the single crystal sample CeIrSi-S1 has been measured in zero magnetic fields using the thermal relaxation method as discussed in section 3.4. Fig. 5.9a shows the decreasing heat capacity over a temperature range from 260 K to 2 K with a maximum of 72.4 J/(mol K) and a minimum of 1.76 J/(mol K) at 8.5 K. A sharp jump at the critical temperature $T_C \approx 8$ K, visible in the inset of Fig. 5.9a may indicate a magnetic phase transition as often seen in rare earth compounds containing magnetic ions such as CePdAl [54, 55] or $TbMn_2Ge$ [56].

In the absence of magnetic contributions, the Sommerfeld coefficient $\gamma = 112.2(7)$ mJ/(mol K^2) can be evaluated by plotting C_p/T vs T^2 and using Eq. 22 as shown in Fig. 5.9b. It should be noted that for this compound, the linear behaviour is only present in a small temperature range from 12 to 16.7 K. Therefore, the evaluated values must be treated with caution. Nevertheless, the trend towards an increased Sommerfeld coefficient, indicating strong electronic correlations, can be seen. Furthermore, the slope yields $\beta = 0.698(3)$ mJ/(mol K^4), corresponding to a Debye temperature of $T_D \approx 141$ K.

The electronic heat capacity contribution $C_{el}(T)$ has been evaluated using polycrystalline reference data of the non-magnetic compound LaIrSi from *F. Kneidinger et al.*[12]. Low-temperature $C_{el}(T)/T$ is shown in Fig. 5.10a together with the heat capacity of CeIrSi and the isotypic reference compound LaIrSi, whereas $C_{el}(T)$ is given by subtracting the phonon contribution: $C_{el}(\text{CeIrSi}) = C_p(\text{CeIrSi}) - C_p(\text{LaIrSi})$. The full temperature range

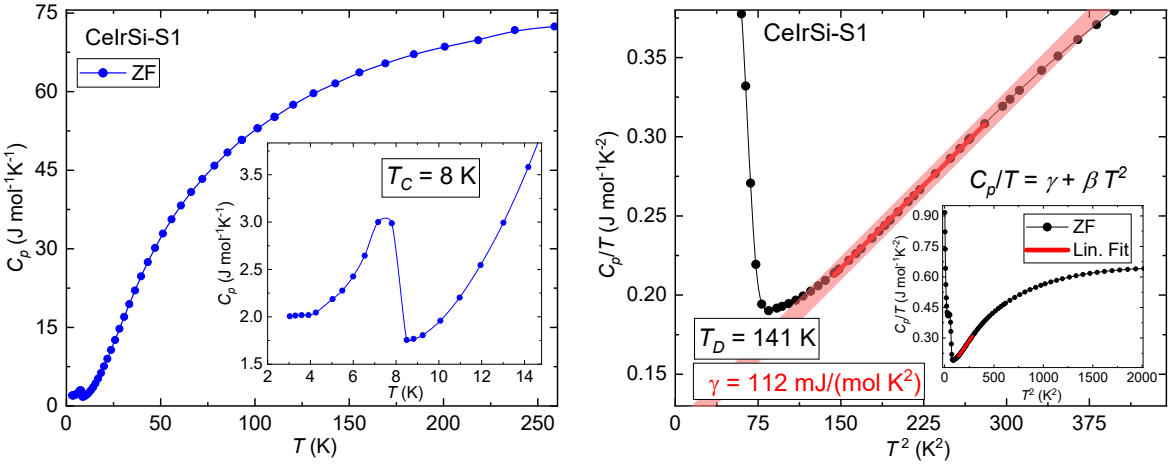

(a) (b)

Figure 5.9: a) Heat capacity as a function of temperature for CeIrSi. The inset shows low-temperature heat capacity with a sharp jump at $T_C = 8\,\mathrm{K}$. b) Heat capacity divided by temperature as a function of T^2. Linear fit to the data by $C_p/T = \gamma + \beta T^2$. The inset shows the full temperature range.

is included in Fig. 5.10a.

The electronic entropy $S_{el}(T)$ can be calculated by integrate $C_{el}/T(T)$ over temperatures [57]:

$$S_{el}(T) = \int_{2\,\mathrm{K}}^{T} \frac{C_{el}(T')}{T'} dT' \tag{27}$$

Furthermore, the theoretic electronic entropy for a Ce^{3+} ion is in the $4f^1$ electron configuration is associated with the total angular momentum $J = 5/2$ and can be evaluated by using [2]:

$$S_{el} = R \ln (g) \tag{28}$$

where R is the universal gas constant and g denotes the degeneration. For a Ce^{3+} ion in cubic symmetry, the sixfold-degenerate $J = 5/2$ state is split by the crystal electric field into a Γ_7 doublet and a Γ_8 quartet [2].

At high temperatures, all energy levels may be occupied and therefore $S_{el}(\Gamma_7 + \Gamma_8) = R \ln (6) = 14.9\,\mathrm{J/(mol\,K)}$. At low temperatures, a possible ground state is the Γ_7 doublet Γ_7, which yields $S_{el} = R \ln (2) = 5.76\,\mathrm{J/(mol\,K)}$ [2, 58], as indicated on the right y-axis in Fig. 5.10b.

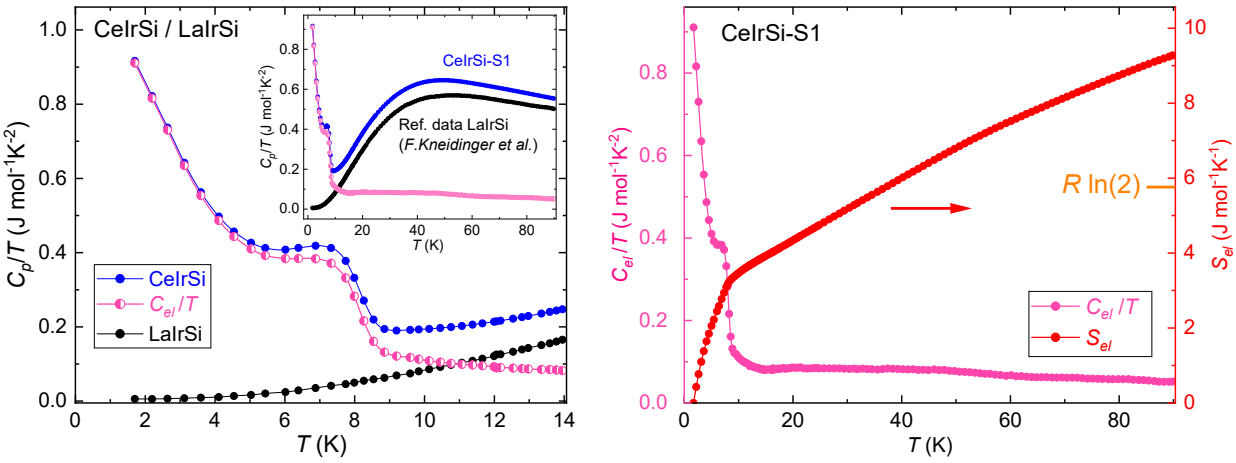

(a) (b)

Figure 5.10: a) Heat capacity divided by Temperature as a function of temperature for CeIrSi, reference data LaIrSi (*F. Kneidinger et al.*[12]) and electronic contribution to the heat capacity of CeIrSi. The inset shows the full temperature range. b) Electronic heat capacity divided by Temperature as a function of temperature for CeIrSi on the left y-axis. Electronic entropy as a function of temperature displayed on the right y-axis. The marker on the right y-axis shows the value of $S_{el} = R \ln 2$ for a free Ce^{3+} ion in the ground state at lowest temperatures.

5.4 Magnetic properties

The temperature-dependent magnetic susceptibility, $\chi = M/H$, was measured in applied fields of 1 T and 3 T parallel to the crystallographic a direction for the CeIrSi-S1 sample, covering the temperature range from 2 K to room temperature. The results are shown in Fig. 5.11a (left y-axis). The CeIrSi single crystal exhibits typical paramagnetic behaviour, with an increase in magnetic susceptibility at lower temperatures.

An anomaly in the inverse susceptibility is observed below $T \approx 20$ K, indicating a magnetic phase transition, as the data deviate from the linear Curie-Weiss law [59]:

$$\frac{1}{\chi} = \frac{T}{C} - \frac{\theta_{CW}}{C} \tag{29}$$

where C is the Curie constant and θ_{CW} is the Curie-Weiss temperature. The data above $T \approx 50$ K can be fitted to this model, yielding a negative Curie-Weiss temperature of

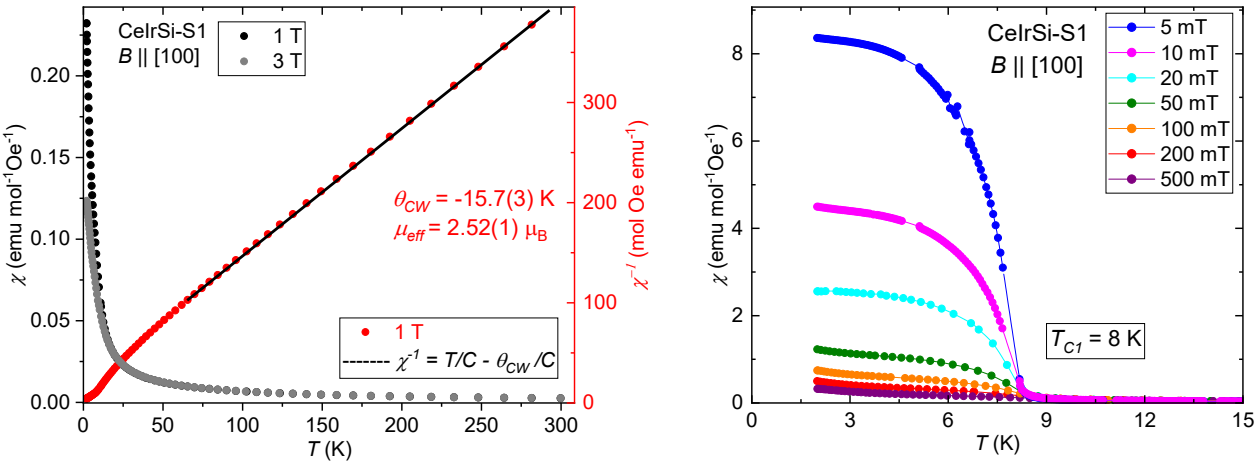

(a) (b)

Figure 5.11: a) Temperature depended magnetic susceptibility of CeIrSi (left y-axis) in applied field of 1 and 3 T and inverse susceptibility (right y-axis) in an applied field of 1 T parallel to [100]. The inverse susceptibility at temperatures above 50 K, can be described by the Curie-Weiss law. b) Low-temperature magnetic susceptibility for several fields applied parallel to [100] shows magnetic ordering below $T_C = 8\,\mathrm{K}$.

$\theta_{CW} = -15.7(3)\,\mathrm{K}$, which indicates dominating antiferromagnetic interactions between Ce^{3+} ions. The effective magnetic moment, determined from the Curie constant, is calculated as [59]:

$$\mu_{eff} = 800\sqrt{C}\ \mu_B \tag{30}$$

This gives $\mu_{eff} = 2.52(1)\,\mu_\mathrm{B}$, which agrees well with both experimental observations $\mu_{eff} = 2.53\,\mu_\mathrm{B}$[12] and the theoretical prediction of $\mu_{calc} = 2.54\,\mu_\mathrm{B}$ for Ce^{3+} with $J = 5/2$ and a Landé g-factor of $g_J = 6/7$.

Low-temperature magnetic susceptibility measurements in fields ranging from 5 mT to 500 mT, parallel to the a direction, are shown in Fig. 5.11b. A steep increase in low-field susceptibility at $T_C = 8\,\mathrm{K}$ indicates a second-order phase transition from a paramagnetic to a magnetically ordered state. This critical temperature is consistent with that, detected in the heat capacity (see Fig. 5.9a). Additionally, an anomalous increase is observed below 3 K for fields exceeding 20 mT.

5.4.1 Magnetization

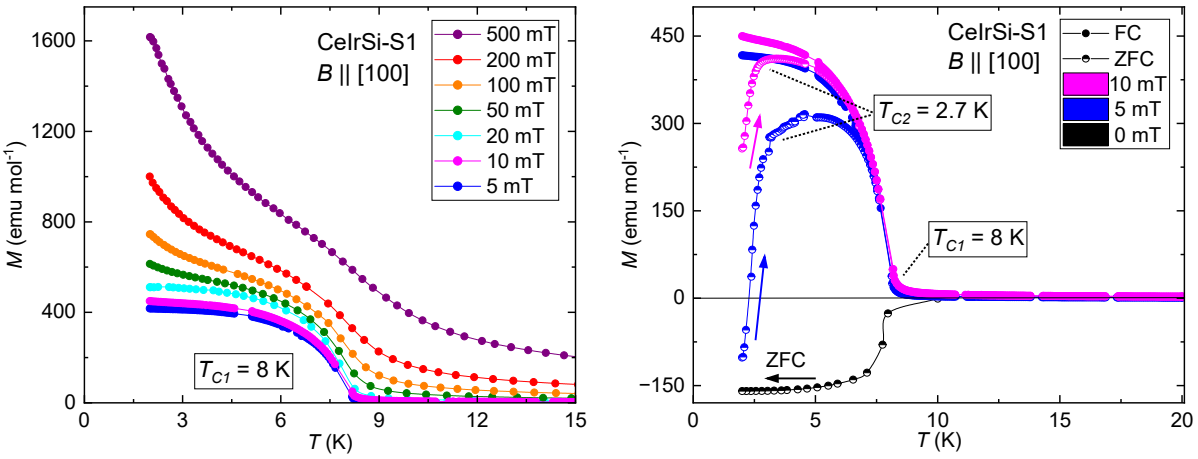

(a) (b)

Figure 5.12: a) Low-temperature dependent magnetization in several magnetic fields applied parallel to [100] of CeIrSi b) Low-temperature dependent magnetization shows significant difference in FC and ZFC curves at 5 mT and 10 mT.

The temperature-dependent magnetization reveals a more pronounced anomaly between 2 K and 4 K (similar to that observed in low-temperature magnetic susceptibility), as shown in Fig. 5.12a. Combined with magnetization measurements under zero-field cooling (ZFC) conditions at 0 mT, 5 mT, and 10 mT (see Fig. 5.12b), this anomaly defines a second critical temperature at approximately $T_{C2}(10\,\mathrm{mT}) \approx 2.7\,\mathrm{K}$.

A significant divergence between the FC and ZFC magnetization curves is observed. In low fields, the magnetic moments may not fully align with the external field in the ZFC state below 2 K. This behaviour suggests the presence of at least two distinct magnetic orderings, occurring below the critical temperatures $T_{C1} = 8\,\mathrm{K}$ and $T_{C2} = 2.7\,\mathrm{K}$, which are defined as magnetic phases 1 and 2, correspondingly.

Fig. 5.13a presents the low-temperature, field-dependent magnetization for five temperatures between 2 K and 10 K. At 2 K, CeIrSi notes a maximal magnetic moment of $M = 0.86\,\mu_B/\mathrm{Ce}$. Below 8 K, the magnetization shows a characteristic increase. Furthermore, hysteresis loops are observed around $B = \pm 50\,\mathrm{mT}$ at temperatures of 2 K and 4 K, which are characteristic for materials with ferromagnetic contributions, as shown in the inset of Fig. 5.13a.

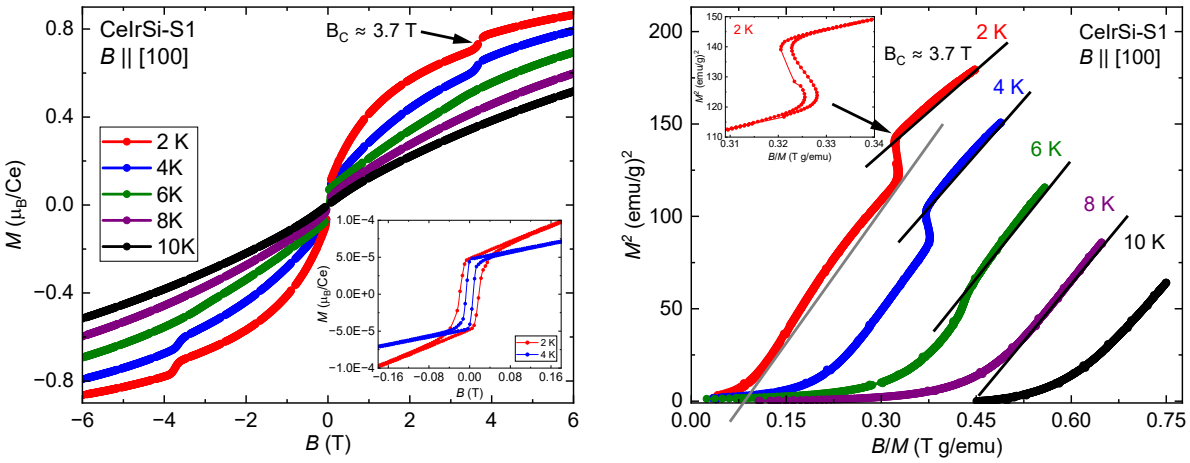

(a) (b)

Figure 5.13: a) Field dependent low temperature magnetization of CeIrSi in units of μ_B per atom Ce with external field applied parallel to [100]. The inset shows hysteresis loops for 2 and 4 K. b) Arrott plot of CeIrSi for five different temperatures between 2 and 10 K.

At temperatures below 8 K a step develops at $B_C(2\,\mathrm{K}) \approx 3.7\,\mathrm{T}$, indicating a field-induced transition from ferromagnetic-like phase 1 to a second phase, referred to as phase 3.

Arrott plots are a well-established method for analyzing magnetic properties and identifying ferromagnetic order in materials [60].

The isothermal plots exhibits linear behaviour at higher fields, which is characteristic for ferromagnetic-like materials, as indicated by the black straight lines in Fig. 5.13b. A pronounced anomaly is observed in the decreasing-field isotherms at $B_C(2\,\mathrm{K}) \approx 3.7\,\mathrm{T}$ corresponding to the step-like feature seen in Fig. 5.13a. This anomaly likely indicates a field-induced transition from a ferromagnetic-like phase 1 to a collinear ferromagnet (phase 3). Below the critical transition field B_C, the Arrott plot exhibits a similar linear behaviour, further supporting the ferromagnetic-like character of phase 1. However, at 2 K the curve already deviates from linearity, which may indicate non-ferromagnetic contributions.

5.4.2 Magnetic anisotropy

Low-temperature magnetization has also been measured for the sample CeIrSi-S2 with fields applied parallel to the crystallographic direction [110]. Fig. 5.14a & 5.14b shows a significant anisotropy in the absolute value of the FC and ZFC magnetization but not in the behaviour. Subtracting the magnetization for the applied field in different crystallographic directions [100] and [110] reveals $\Delta M(4\,\mathrm{K}) \approx 170\,\mathrm{emu/mol}$ at 4 K, while the critical temperatures do not change.

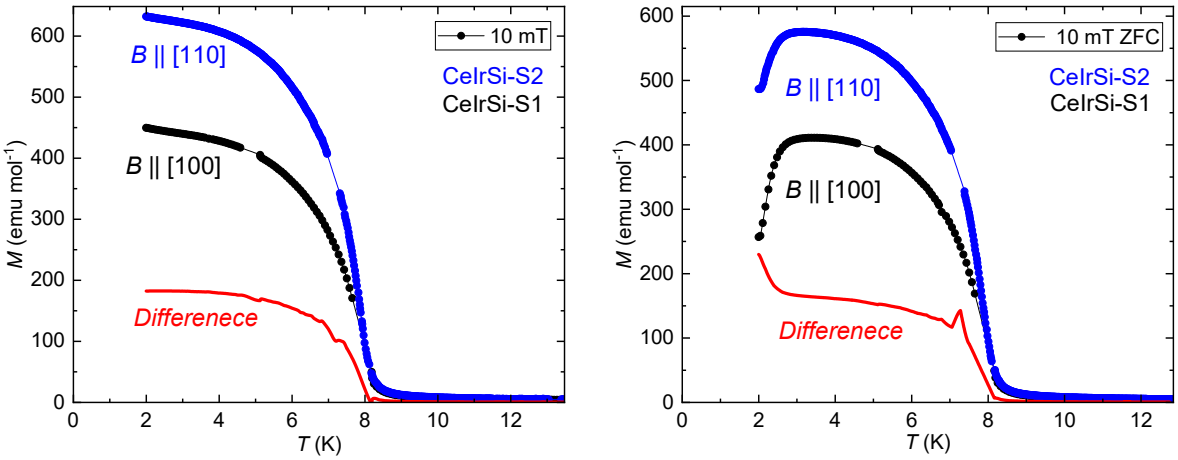

(a) (b)

Figure 5.14: Low-temperature magnetization of CeIrSi for a magnetic field of 10 mT applied parallel to [100] and [110]. The red curve shows the degree of anisotropy for an external magnetic field applied to different crystallographic directions. a) Field cooling b) Zero field cooling

5.5 Electrical resistivity

The temperature-dependent electrical resistivity $\rho(T)$ of CeIrSi, measured from 2 K to room temperature, exhibits semimetallic behaviour, as shown in Fig. 5.15a. The resistivity reaches a maximum value of 372 µΩcm at 250 K. The deviation from simple metallic behaviour at high temperatures, characterized by a continuously decreasing curvature, may be attributed to the thermal population of higher-energy crystal electric field (CEF) levels, a common phenomenon in Ce-based compounds [2, 12, 61, 62]. At $T_C = 8\,\mathrm{K}$, the

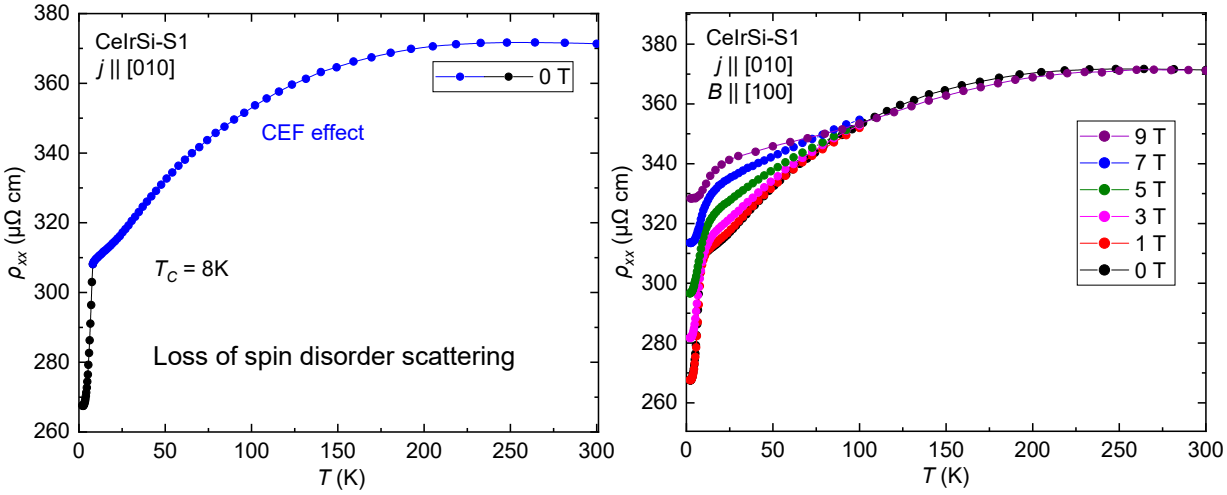

(a) (b)

Figure 5.15: a) Temperature dependent resistivity of CeIrSi with current parallel to [010] b) Temperature dependent resistivity of CeIrSi in external magnetic fields perpendicular to the current.

resistivity experiences a sharp drop from 308 to 267 µΩcm, corresponding to a decrease of approximately 12%, after which it tends to saturate. This significant reduction in resistivity corresponds to the magnetic phase transition observed in heat capacity and magnetic susceptibility measurements. It is likely associated with the reduction of spin-disorder scattering due to the alignment of magnetic moments.

The low-temperature resistivity increases with increasing external fields up to 9 T, as shown in Fig. 5.15b. In contrast, external fields have no significant effect on the resistivity above 100 K.

A comparison with literature data by *F. Kneidinger et al.*[12] for polycrystalline CeIrSi reveals a similar decreasing curvature, attributed to CEF effects on the energy levels. The resistivity of the single-crystalline sample at 140 K is significantly higher (363 µΩcm) compared to that of the polycrystalline sample (303 µΩcm).

However, the resistivity of the polycrystalline sample reaches a maximum at approximately 140 K, significantly lower than that of the single-crystal sample. Additionally, the drop in resistivity at low temperatures due to magnetic ordering is less pronounced. A notable difference is observed in the behaviour under magnetic fields, while the resistivity

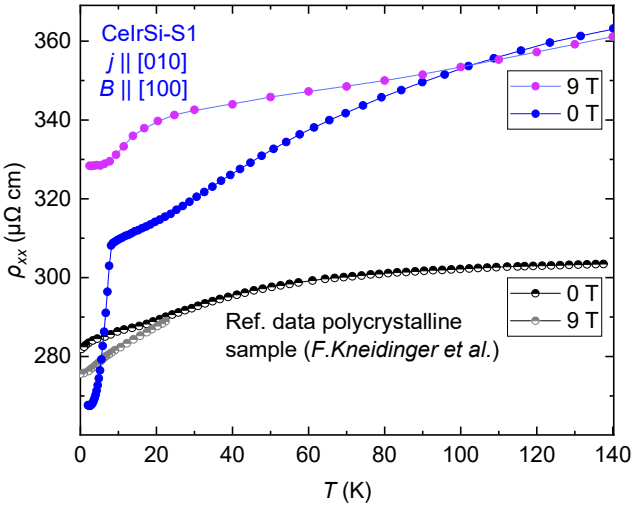

Figure 5.16: Comparison of temperature-dependent resistivity in zero field and 9 T between polycrystalline samples (*F. Kneidinger et al.*[12]) and single-crystal CeIrSi.

decreases in external fields for the polycrystalline sample, it increases in the single-crystal sample.

5.5.1 Anisotropic electrical resistivity

Temperature-dependent resistivity measurements with current parallel to the [110] direction for the sample CeIrSi-S2 reveal a significantly higher resistivity value at room temperature of 546 µΩcm and 365 µΩcm respectively, as shown in Fig. 5.17a. The resistivity increases with decreasing temperature, indicating semiconducting behaviour. A small hump around 50 K may still be attributed to CEF effects, while the sharp increase at approximately 10 K is likely associated with magnetic ordering at low temperatures. Similar to the polycrystalline sample, the resistivity decreases under the influence of external fields.

The pronounced anisotropy in resistivity between different crystallographic directions is highlighted by the normalized resistivity relative to that at room temperature for the (100) and (110) directions, as shown in Fig. 5.17b.

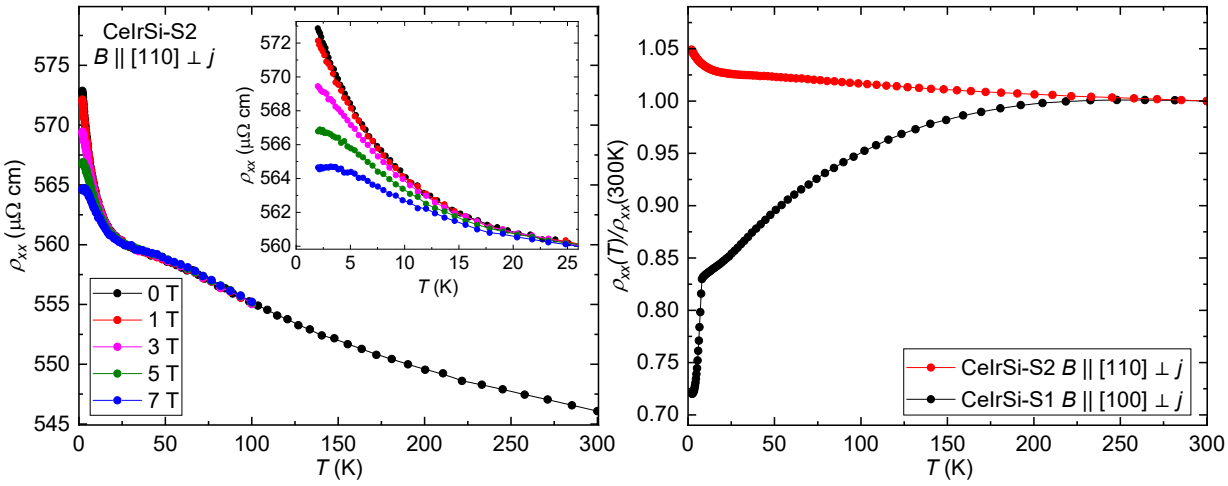

(a) (b)

Figure 5.17: a) Electrical resistivity of CeIrSi measured with current perpendicular to the [110] direction across the full temperature range from 2 K to room temperature. The inset displays the resistivity under external magnetic fields up to 7 T. b) Temperature-dependent normalized resistivity, comparing the crystallographic directions [100] and [110].

5.6 Field-dependent resistivity

The field-dependent resistivity of CeIrSi, with current applied parallel to a, was measured at several temperatures ranging from 1.85 K to 8 K in external fields between −5 T and 5 T. As shown in Fig. 5.18a, the symmetric signal exhibits a pronounced anomaly that becomes more distinct with decreasing temperature, centered around $B = 3.76$ T (and −3.76 T, respectively) at 2 K. This anomaly aligns well with the field-induced transition from phase 1 to a ferromagnetic state, as observed in the field-dependent magnetization and the Arrott plot discussed in Section 5.4.1. Additionally, the critical magnetic field $B_C(T)$ increases with decreasing temperature, as illustrated in Fig. 5.18b.

Similar to the hysteresis observed in the magnetization, the field-dependent resistivity also exhibits hysteresis loops below 3.5 K at the field-induced transition.

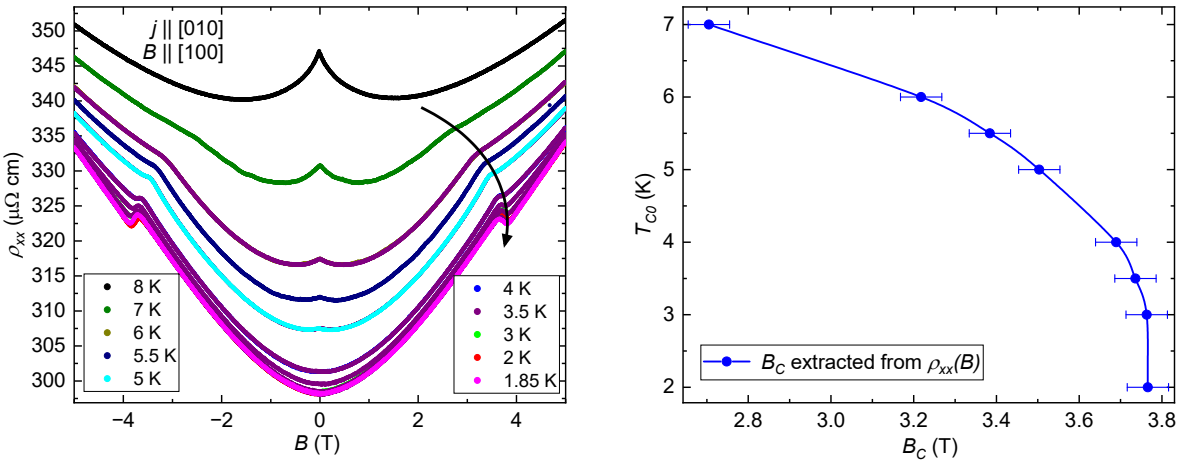

(a) (b)

Figure 5.18: a) Field-dependent resistivity of CeIrSi measured at various temperatures between −5 T to 5 T. b) Temperature dependence of the critical magnetic field associated with the transition observed in the field-dependent resistivity of CeIrSi.

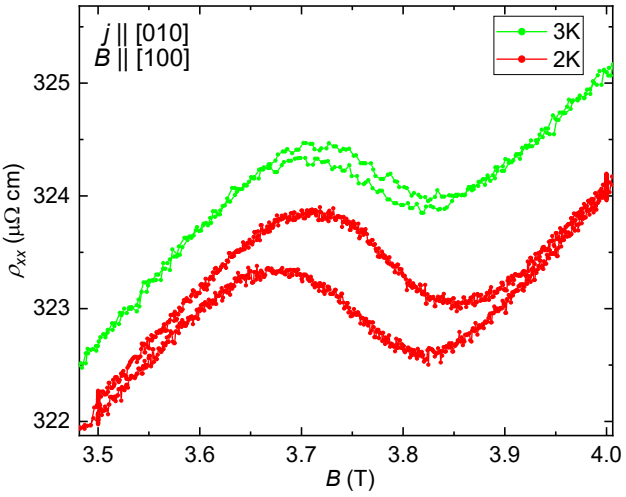

Figure 5.19: Hysteresis in the field-dependent resistivity of CeIrSi at the field induced transition.

5.7 Hall effect

The field dependent Hall effect for the sample CeIrSi-S1 has been measured for several temperatures from 1.85 K to 8 K. The raw data in Fig. 5.20a, show an increasing strong

non-linear behaviour for falling temperatures below 8 K between −3.76 T and 3.76 T according to the transition field evaluated in field-dependent resistivity and magnetization measurements. Additionally, a hump is observed at 1.85 K and 2 K between −1.5 T and

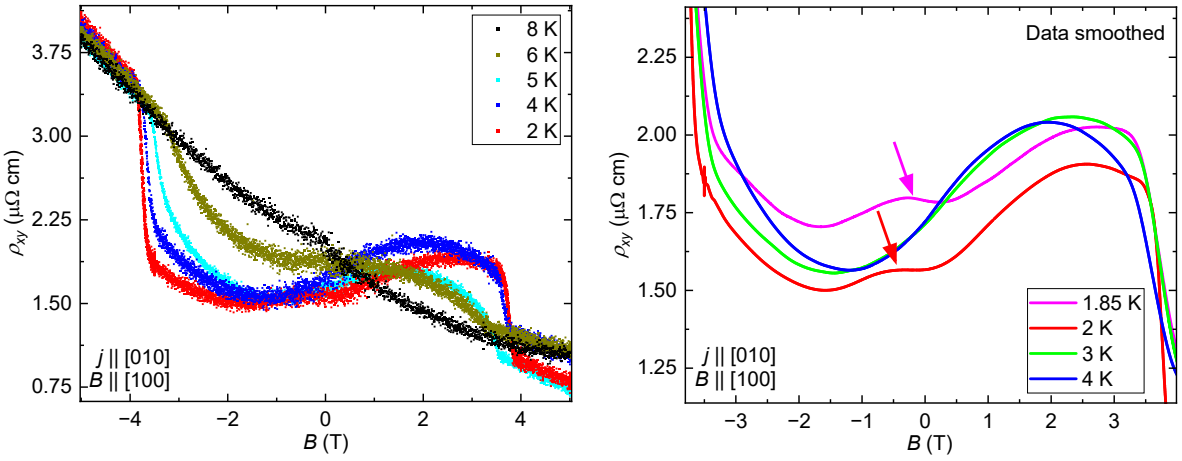

(a) (b)

Figure 5.20: a) Low-temperature Hall resistivity as function of magnetic field with current parallel to a and magnetic field perpendicular to a b) Smoothed Hall resistivity with a hump at 1.85 and 2 K.

0.5 T (Fig. 5.20b), which may be linked to the phase transition from phase 1 to phase 2 detected in magnetic susceptibility and magnetization measurements below $T_{C2} = 2.7$ K (see Fig. 5.11b & Fig. 5.12a).

Apart from the pronounced non-linear behaviour below 8 K within the field range of −3.76 T to 3.76 T, non-linearity is also evident in the Hall data at 8 K (Fig. 5.21a). Furthermore, strong asymmetry is observed in measurements conducted at 4 K between ±12 T (Fig. 5.21b). The red curve serves as a visual guide, helping to see the absence of the anomalous behaviour below 3.7 T. The orange straight line highlights the deviation from a linear Hall effect.

The pronounced anomalous behaviour below 3.7 T (−3.7 T, respectively), which aligns well with the critical magnetic field $B_C(T)$ observed in magnetization measurements, may be at least partially attributed to the anomalous Hall effect in the phase 1 induced by magnetic ordering. To isolate the anomalous Hall contribution ρ_{xy}^{AH} the red reference curve, serving as a guide for the eye, was taken as a baseline $\rho_{xy}^{baseline}$ for the Hall data (see Fig. 5.22a). Notably, the extracted anomalous Hall effect exhibits an asymmetric

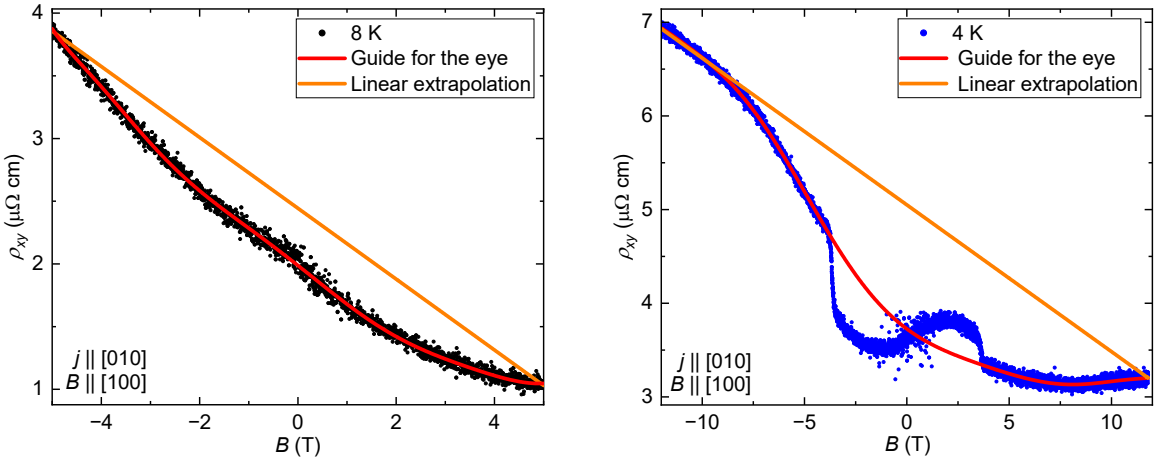

(a) (b)

Figure 5.21: a) Hall resistivity as function of magnetic field at 8 K. The red curve serves as guide for the eye and a linear extrapolation shows the non-linearity of the Hall effect. b) Hall resistivity as a function magnetic field up to ±12 T at 4 K. The red curve serves as guide for the eye and a linear extrapolation shows the non-linearity of the Hall effect.

strength, nearly doubling in the negative magnetic field range at 2 K.

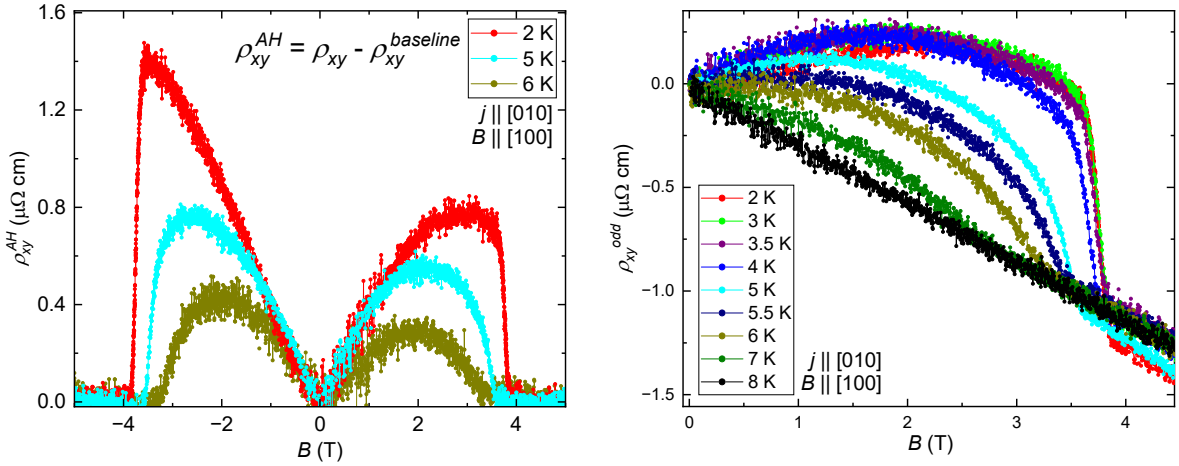

(a) (b)

Figure 5.22: a) Anomalous Hall resistivity as function of magnetic field evaluated by subtracting the pseudo linear part ρ_{xy}^{linear}. b) Antisymmetrized Hall resistivity as function of magnetic field.

For further analysis, the raw Hall data ρ_{xy} were antisymmetrized, ρ_{xy}^{odd}, to eliminate contributions from the longitudinal resistivity, as shown in Fig. 5.22b. The charge carrier concentration is determined from the slope of a linear fit to $\rho_{xy}^{odd}(8\,\mathrm{K})$ (Fig. 5.23). The negative slope indicates electrons as the dominant charge carriers, with a concentration of $n = 2.176(2) \times 10^{21}/\mathrm{cm}^3$.

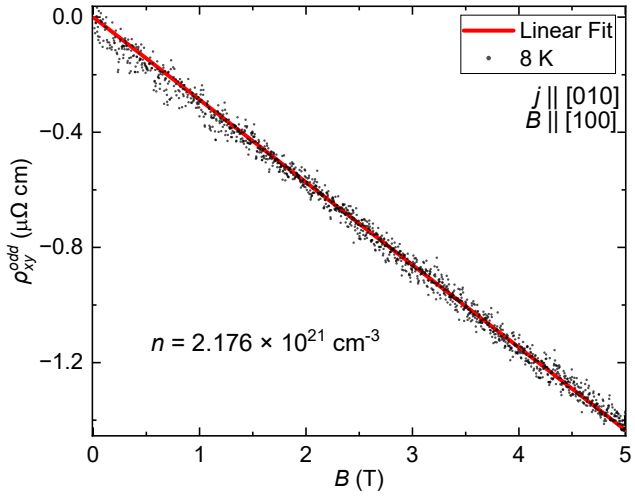

Figure 5.23: Linear fit for the odd-in-field Hall resistivity at 8 K to evaluate the charge carrier concentration.

The antisymmetrized Hall data are fitted above 3.7 T and extrapolated to zero field to approximate the linear Hall contribution in the whole field range (see Fig. 5.24a). This linear component is then subtracted to isolate the anomalous Hall contribution $\rho_{xy,odd}^{AH}$ at each temperature, as shown in Fig. 5.24b.

A distinct form is observed in the pure symmetrized Hall signal ρ_{xy}^{even}, when subtracting the symmetrized longitudinal resistivity $\rho_{xx}^{even,meas.}$ scaled by α from the symmetrized Hall resistivity $\rho_{xy}^{even,meas.}$ as shown in Fig. 5.25. A step-like feature emerges as the material is cooled, with the step located at the critical field B_C.

Finally, Fig. 5.26 presents the temperature-dependent Hall resistivity measured between 2 and 40 K at zero field, 1, 3.7, and 7 T. In the absence of a magnetic field, the Hall resistivity exhibits a sharp drop at $T_{C1} = 8\,\mathrm{K}$, possibly marking the transition to a magnetically ordered state. This critical temperature is also in good agreement with the values obtained from heat capacity and magnetization measurements.

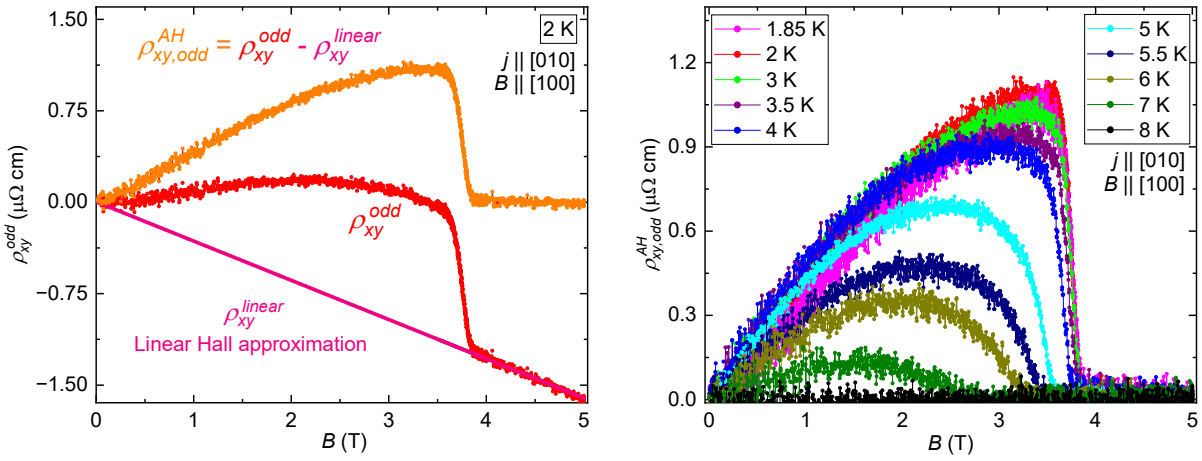

(a) (b)

Figure 5.24: a) Illustration for the evaluation of the anomalous Hall resistivity (orange) from the odd-in-field resistivity (red) at 2 K. The linear Hall approximation is shown in pink. b) Calculated anomalous Hall resistivity for several temperatures.

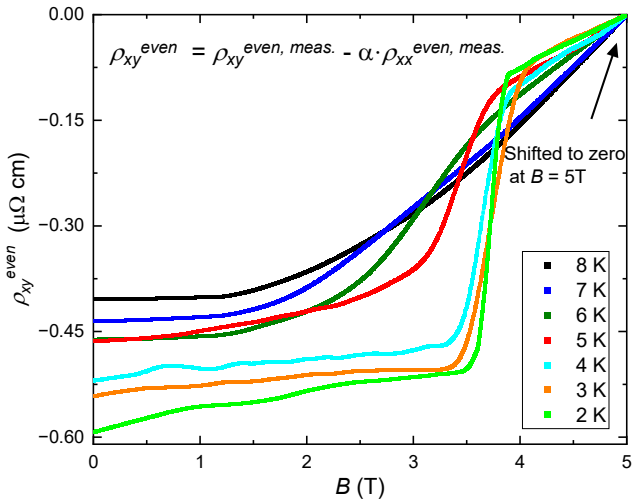

Figure 5.25: Symmetrized Hall resistivity smoothed and scaled to the even-in-field curve of 8 K at 5 T.

At 1 T, ρ_{xy} exhibits a dip at a slightly higher temperature of 8.2 K, defined as $T_{C0,1}$, followed by a sharp peak at $T_{C2} = 3.7$ K. This second critical temperature may be related to the magnetic ordering of phase 2 observed at the lowest temperatures in FC

and ZFC magnetization measurements (see Fig. 5.12a & 5.12b).

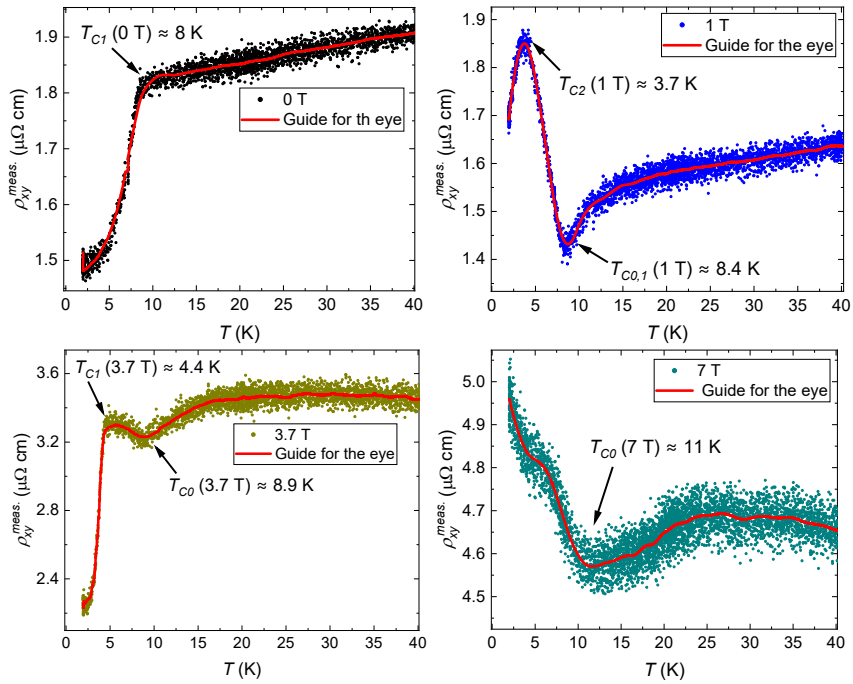

Figure 5.26: Low-temperature Hall resistivity of CeIrSi in the field of 0, 1, 3.7, and 7 T applied parallel to [100]. Kink and humps indicate magnetic transitions, T_{C0} standing for transition to ferromagnetic, T_{C1} to phase 1 and T_{C3} to phase 2.

The peak observed in the Hall resistivity at 4.4 K in a 3.7 T field aligns well with the critical temperature of 4.1 K at $B_C = 3.7$ T from field-dependent resistivity (Fig. 5.18b), which marks the transition to a collinear ferromagnetic state. Consequently, the dip at $T_{C0} = 8.9$ K signifies the transition from the paramagnetic to the ferromagnetic state, which shifts to higher temperatures with increasing magnetic field.

At higher fields of 7 T, this transition temperature increases to 11 K. The small hump around 5 K cannot be associated with any of these transitions.

6 Discussion

This section focuses on the magnetic ordering at low temperatures by summarizing the collected data in a comprehensive phase diagram and analyzing the low-temperature phases observed in heat capacity, magnetization, and electrical transport measurements.

CeIrSi was initially selected as a candidate material because of its proposed classification as a non-magnetic Kramers Weyl Kondo semimetal. In particular, *Kneidinger et al.* [12] reported non-magnetic behaviour in polycrystalline samples of CeIrSi.

A central experimental method employed in this study to probe the potential topological properties of CeIrSi is the Hall effect measurement. These reveal a pronounced non-linear contribution, which will be examined in detail, especially in relation to possible contributions from magnetic ordering at low temperatures.

6.1 Magnetic ordering

Magnetic susceptibility measurements reveal a high-temperature Curie–Weiss paramagnetic behaviour with a negative Curie–Weiss temperature, suggesting the presence of dominant antiferromagnetic interactions. In contrast, low-temperature measurements of heat capacity, magnetization, and electrical transport uncover the emergence of complex magnetic ordering below $T_{C1} \approx 8\,\mathrm{K}$, with a collinear ferromagnetic state developing under applied magnetic fields, as illustrated in Fig. 6.1. The phase diagram is constructed based on data from heat capacity, magnetization, and electrical transport measurements.

CeIrSi crystallizes in the non-centrosymmetric cubic structure $P2_13$, a structure type that can be considered as a three-element version of the compound family $B20$, usually related to binary systems. This class of materials is renowned for hosting chiral magnetic orders, such as spiral and topologically non-trivial spin textures, as observed in canonical systems like FeGe [63], MnSi [64], and $Fe_{1-x}Co_xSi$ [65].

Magnetic phase diagrams of these B20 compounds are typically governed by competition between ferromagnetic exchange interactions and the Dzyaloshinskii-Moriya interaction (DMI) [66]. At zero or low magnetic fields, this interplay stabilizes a helical magnetic

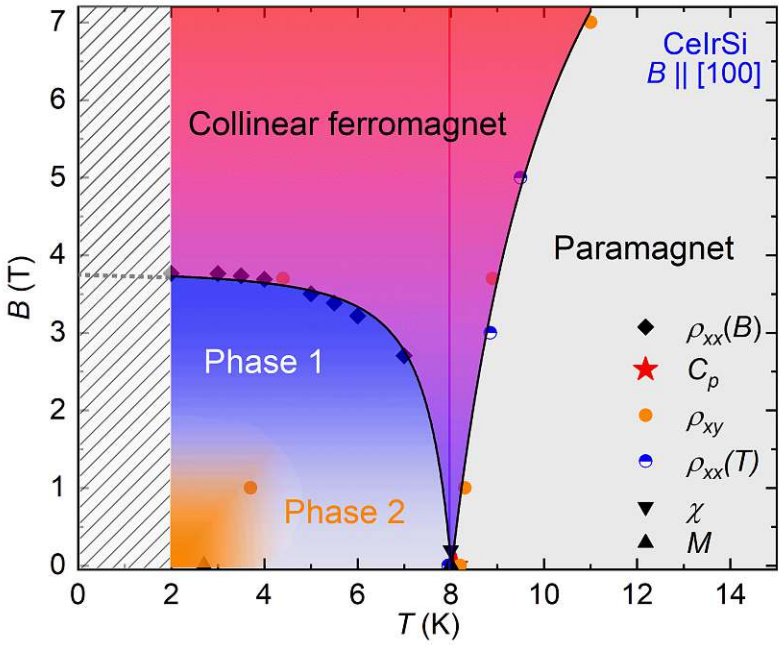

Figure 6.1: Magnetic phase diagram of CeIrSi as a function of temperature, constructed from heat capacity, magnetization, and electrical transport measurements.

phase. Upon applying a finite magnetic field, the system transitions into a conical phase, where the magnetic moments partially align along the field direction while preserving a helical component. At higher magnetic fields, the spins align uniformly along the field direction, resulting in a collinear ferromagnetic phase. In addition, within specific ranges of temperature and magnetic field, topologically protected spin textures can emerge in the form of a skyrmion lattice. These skyrmion phases have been experimentally observed, for instance, in MnSi (Fig. 6.2a) [64] and FeGe (Fig. 6.2b) [67].

In analogy to the well-studied $B20$ material class, it may be plausible that the distinct magnetic phase, denoted as phase 2 (orange-shaded region in Fig. 6.1), which emerges below approximately 4 K, originates from a helical magnetic state. In this scenario, pairs of Ce atoms in a non-centrosymmetric environment may adopt a non-collinear spin alignment due to the Dzyaloshinskii–Moriya interaction, leading to the formation of a helical spin structure.

The blue-shaded region below 8 K, referred to as phases 1, may correspond to a conical magnetic phase. However, the precise nature of the magnetic phases observed in phases 1

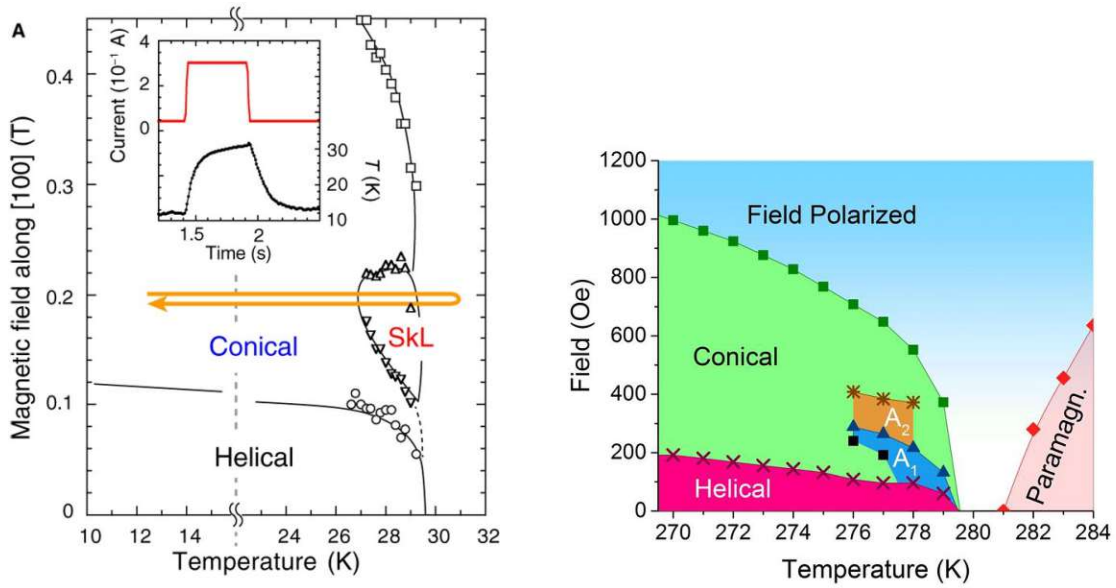

(a) (b)

Figure 6.2: a) Phase diagram of the B20 compound MnSi, showing the characteristic helical and conical magnetic phases, along with the formation of a skyrmion lattice (SKL) in a distinct region of the temperature–field space [64]. b) Phase diagram of the B20 compound FeGe, exhibiting typical helical and conical spin textures, as well as skyrmion lattice phases labeled A_1 and A_2, corresponding to specific pockets within the phase space [67].

and 2 remains speculative. Notably, phase 2 could also correspond to a skyrmion lattice, although a conclusive identification is not possible with the current dataset. Additionally, this compound is known to exhibit magnetic frustration, arising from the trillium lattice geometry formed by the Ce atoms. Such a configuration could lead to non-trivial magnetic states as well.

To clarify the underlying magnetic ordering, neutron scattering would be an ideal technique, as it allows direct probing of spin structures in reciprocal space, as performed for MnSi [66]. Additionally, detailed magnetic property measurements below 2 K are essential to fully capture the low-temperature regime.

6.2 Anisotropy

The availability of a single crystal enabled the investigation of anisotropic properties. Our measurements showed that the cubic chiral compound CeIrSi exhibits pronounced

anisotropy in its electrical resistivity. Along the crystallographic direction [100], CeIrSi displays semimetallic behaviour with reduced resistivity under applied magnetic fields. In contrast, measurements along the [110] direction reveal semiconducting behaviour, with resistivity increasing in the presence of an external magnetic field. Furthermore, reference measurements by *F.Kneidinger et al.*[12] on polycrystalline samples of CeIrSi revealed a similar semimetallic character as observed in the [100] direction. The resistivity increases with applied magnetic fields, similar to the trend seen in the [110] direction. This suggests that the resistivity of the polycrystalline sample just averages the contributions from all crystallographic directions. Furthermore, magnetic anisotropy is also evident in the magnetization data, with the magnetization along the [110] direction being approximately 30% higher than along [100].

Measurement of various physical properties along the screw axis 2_1 oriented in the crystallographic direction [111], may be highly promising to reveal pronounced anisotropy, as this axis is directly associated with the intrinsic chirality of the crystal structure.

6.3 Non linear Hall effect

The presented Hall data exhibit a pronounced non-linearity, which could potentially be attributed to a spontaneous Hall effect originating from the Berry curvature, although this interpretation is not definitive. Alternatively, a more straightforward explanation may lie in the complex underlying magnetic structure discussed in the previous section 6.1.

On one hand, the Hall effect observed below 8 K may primarily originate from an anomalous contribution associated with magnetic phases. On the other hand, Skyrmions are known to exhibit topological features [68] that can lead to a non-trivial Berry curvature, giving rise to a spontaneous Hall effect.

To identify the contributions of Berry curvature to the non-linear Hall effect (NLHE) arising from Weyl points, two approaches can be taken:

First, focussing on the strong NLHE at low temperatures in the complex magnetically ordered regime. Hence, a complete understanding of the magnetic phases is essential to attribute portions of the NLHE to either conventional anomalous mechanisms originating from magnetic ordering or topological origins arising from Skyrmions or Kramers-Weyl

points.

Second, by focussing on the paramagnetic regime above 8 K and the collinear ferromagnetic state at higher magnetic fields (see Fig. 6.1). Measuring the Hall response in the paramagnetic regime will identify whether any non-linear Hall contribution persists in the absence of long-range magnetic order. If only an ordinary Hall effect is observed, it can be clearly extracted and used as a baseline in the collinear ferromagnetic regime. Since the magnetic structure in the ferromagnetic regime is well characterized, the anomalous Hall contribution to the NLHE could be reliably distinguished. This allows for a separation of ordinary and anomalous contributions, potentially uncovering topological contributions from Berry curvature associated with Kramers-Weyl points.

7 Summary and Outlook

The aim of this thesis was the single crystal growth and physical characterization of the chiral cubic compound CeIrSi. Due to its chiral crystal structure, strong spin-orbit coupling, and signatures of strong electronic correlations in the heat capacity, CeIrSi has been proposed as a promising candidate for a Kramers-Weyl Kondo semimetal. To probe its potential topological properties, Hall effect measurements were performed as a key experimental approach.

A high-quality, impurity-free single crystal with high stoichiometry was grown successfully for the first time using the optical floating zone method. Two oriented samples, aligned along the [100] and [110] crystallographic directions, were used for heat capacity, magnetization, and electrical transport measurements. Heat capacity measurements revealed an enhanced Sommerfeld coefficient, indicating strong electronic correlations. Electrical transport measurements revealed strong anisotropy, with semimetallic behaviour along the [100] direction and semiconducting behaviour along the [110] direction.

While the material has a paramagnetic behaviour down to 8 K, heat capacity, magnetization, and electrical transport measurements, including field-dependent resistivity, reveal multiple phase transitions at lower temperatures. This stands in clear contrast to previous studies on polycrystalline samples, which reported the compound to be non-magnetic [12]. Two magnetic phases 1, and 2 were found below 8 K in small external magnetic fields with complex magnetic ordering. While the precise nature of the ordering remains unresolved,

the behaviour is reminiscent of helimagnetic and conical magnetic structures, typically seen in related B20 compounds. This assumption is further supported by the collinear ferromagnetic state arising at higher magnetic fields. However, a skyrmion lattice phase cannot be excluded.

A key result of this work is the observation of a strong non-linear Hall effect below 8 K. This effect cannot be straightforwardly attributed to Berry curvature contribution alone. Instead, it may arise from the complex magnetic ordering itself. Distinguishing between these possibilities will require further experimental efforts, particularly a detailed determination of the magnetic structures or Hall measurements in the paramagnetic regime, which could serve as a baseline for identifying the non-linear Hall contributions in the collinear ferromagnetic state. Finally, investigations on a single crystal oriented along the screw axis in the [111] crystallographic direction should be considered, as this axis is directly associated with the intrinsic chirality of the structure and may reveal pronounced anisotropic and chiral effects.

List of Figures

References

1. Paschen, S. & Si, Q. Quantum phases driven by strong correlations. *Nature Reviews Physics* **3,** 9–26 (2021).
2. Bühler-Paschen, S., Bauer, E. & Pustogow, A. Strongly Correlated Electron Systems. *Lecture notes, Technische Universität Wien* (2024).
3. Hasan, M. Z. *et al.* Weyl, Dirac and high-fold chiral fermions in topological quantum matter. *Nature Reviews Materials* **6,** 784–803 (2021).
4. Chang, G. *et al.* Topological quantum properties of chiral crystals. *Nature materials* **17,** 978–985 (2018).
5. Huang, S.-M. *et al.* A Weyl Fermion semimetal with surface Fermi arcs in the transition metal monopnictide TaAs class. *Nature communications* **6,** 7373 (2015).
6. Dzsaber, S. *et al.* Giant spontaneous Hall effect in a nonmagnetic Weyl–Kondo semimetal. *Proc. Natl Acad. Sci. USA* **118,** e2013386118 (2021).
7. Singh, B., Lin, H. & Bansil, A. Topology and symmetry in quantum materials. *Advanced Materials* **35,** 2201058 (2023).
8. Nakatsuji, S., Kiyohara, N. & Higo, T. Large anomalous Hall effect in a non-collinear antiferromagnet at room temperature. *Nature* **527,** 212–215 (2015).
9. Ikhlas, M. *et al.* Large anomalous Nernst effect at room temperature in a chiral antiferromagnet. *Nature Physics* **13,** 1085–1090 (2017).
10. Chang, G. *et al.* Unconventional chiral fermions and large topological Fermi arcs in RhSi. *Physical review letters* **119,** 206401 (2017).
11. Klein, M. J. On a degeneracy theorem of kramers. *American Journal of Physics* **20,** 65–71 (1952).
12. Kneidinger, F. *et al.* Physical properties of CeIrSi with trillium-lattice frustrated magnetism. *Physical Review B* **100,** 134442 (2019).
13. Lipatov, A., Gribanov, A. & Dunaev, S. The ternary system cerium–iridium–silicon. *Journal of Alloys and Compounds* **696,** 1019–1030 (2017).
14. Yao, M. *et al.* Observation of giant spin-split Fermi-arc with maximal Chern number in the chiral topological semimetal PtGa. *Nature communications* **11,** 2033 (2020).

15. Sluchanko, N. *et al.* Heavy fermions in CeAl3. *Physica B: Condensed Matter* **378,** 773–774 (2006).

16. Vishwanath, A. Where the Weyl things are. *Physics* **8,** 84 (2015).

17. Pal, P. B. Dirac, majorana, and weyl fermions. *American Journal of Physics* **79,** 485–498 (2011).

18. Vafek, O. & Vishwanath, A. Dirac fermions in solids: From high-T c cuprates and graphene to topological insulators and Weyl semimetals. *Annu. Rev. Condens. Matter Phys.* **5,** 83–112 (2014).

19. Grefe, S. E., Lai, H.-H., Paschen, S. & Si, Q. Weyl-Kondo semimetals in nonsymmorphic systems. *Physical Review B* **101,** 075138 (2020).

20. Ayani, C. G. *et al.* Two-dimensional Kondo lattice in a TaS2 van der Waals heterostructure. *arXiv preprint arXiv:2205.11383* (2022).

21. Getzlaff, M. *Fundamentals of magnetism* (Springer Science & Business Media, 2007).

22. Chen, R. & Wang, N. L. Infrared properties of heavy fermions: evolution from weak to strong hybridizations. *Reports on Progress in Physics* **79,** 064502 (2016).

23. Lai, H.-H., Grefe, S. E., Paschen, S. & Si, Q. Weyl–Kondo semimetal in heavy-fermion systems. *Proceedings of the National Academy of Sciences* **115,** 93–97 (2018).

24. Fecher, G. H., Kübler, J. & Felser, C. Chirality in the solid state: Chiral crystal structures in chiral and achiral space groups. *Materials* **15,** 5812 (2022).

25. Flack, H. D. Chiral and achiral crystal structures. *Helvetica Chimica Acta* **86,** 905–921 (2003).

26. Luo, X., Pu, M., Ma, X. & Li, X. Taming the electromagnetic boundaries via metasurfaces: from theory and fabrication to functional devices. *International Journal of Antennas and Propagation* **2015,** 204127 (2015).

27. Zhang, Y. *et al.* Kramers nodal lines and Weyl fermions in SmAlSi. *Communications Physics* **6,** 134 (2023).

28. De Juan, F., Grushin, A. G., Morimoto, T. & Moore, J. E. Quantized circular photogalvanic effect in Weyl semimetals. *Nature communications* **8,** 15995 (2017).

29. He, W.-Y., Xu, X. Y. & Law, K. T. Kramers Weyl semimetals as quantum solenoids and their applications in spin-orbit torque devices. *Communications Physics* **4,** 66 (2021).

30. Ghimire, N. J. Complex magnetism in noncentrosymmetric magnets (2013).

31. Singh, S. *et al.* Hall effect measurements in the heavy-fermion system CeCoIn5. *Physica B: Condensed Matter* **378,** 821–822 (2006).

32. Siddiquee, H. *et al.* Breakdown of the scaling relation of anomalous Hall effect in Kondo lattice ferromagnet USbTe. *Nature communications* **14,** 527 (2023).

33. Xu, S. *et al.* Universal scaling law for chiral antiferromagnetism. *Nature communications* **15,** 3717 (2024).

34. Hall, E. H. *et al.* On a new action of the magnet on electric currents. *American Journal of Mathematics* **2,** 287–292 (1879).

35. Nair, S. *et al.* Hall effect in heavy fermion metals. *Advances in physics* **61,** 583–664 (2012).

36. Nagaosa, N., Sinova, J., Onoda, S., MacDonald, A. H. & Ong, N. P. Anomalous hall effect. *Reviews of modern physics* **82,** 1539–1592 (2010).

37. Yue, D. & Jin, X. Towards a better understanding of the anomalous Hall effect. *Journal of the Physical Society of Japan* **86,** 011006 (2017).

38. Karplus, R. & Luttinger, J. Hall effect in ferromagnetics. *Physical Review* **95,** 1154 (1954).

39. Jungwirth, T., Niu, Q. & MacDonald, A. Anomalous Hall effect in ferromagnetic semiconductors. *Physical review letters* **88,** 207208 (2002).

40. Zhang, S.-S., Ishizuka, H., Zhang, H., Halász, G. B. & Batista, C. D. Real-space Berry curvature of itinerant electron systems with spin-orbit interaction. *Physical Review B* **101,** 024420 (2020).

41. Xiao, D., Chang, M.-C. & Niu, Q. Berry phase effects on electronic properties. *Reviews of modern physics* **82,** 1959–2007 (2010).

42. Benz, K.-W. & Neumann, W. *Introduction to crystal growth and characterization* (John Wiley & Sons, 2014).

43. Nishinaga, T. *Handbook of crystal growth: fundamentals* (Elsevier, 2014).

44. Dinnebier, R. E. & Billinge, S. J. *Powder diffraction: theory and practice* (Royal society of chemistry, 2008).

45. Bragg, W. H. & Bragg, W. L. *X rays and crystal structure* (G. Bell and Sons, Ltd., 1915).

46. Hidayanti, F. & Harnovan, A. A. Application of scanning electron microscopy: a review. *International Journal of Applied Science and Engineering Review* **1,** 91–102 (2020).

47. Goldstein, J. I. *et al. Scanning electron microscopy and X-ray microanalysis* (springer, 2017).

48. Schmehr, J. L. & Wilson, S. D. Active crystal growth techniques for quantum materials. *Annual Review of Materials Research* **47,** 153–174 (2017).

49. Manual, H. C. O. U. Physical Property Measurement System. *Citado* **2,** 11 (2002).

50. Rosen, P. F. & Woodfield, B. F. Standard methods for heat capacity measurements on a quantum design physical property measurement system. *The Journal of Chemical Thermodynamics* **141,** 105974 (2020).

51. Design, Q. Vibrating Sample Magnetometer (VSM) Option User's Manual. *Quantum Design* **6325** (2011).

52. Shukla, V. in *Handbook of Magnetic Hybrid Nanoalloys and their Nanocomposites* 483–505 (Springer, 2022).

53. Heying, B. *et al.* Synthesis, Structure, and Magnetic Properties of the Silicides RE IrSi (RE= Ce, Pr, Er, Tm, Lu) and SmIr 0.266 (8) Si 1.734 (8). *Monatshefte für Chemie/Chemical Monthly* **135,** 1335–1347 (2004).

54. Fritsch, V. *et al. CePdAl-a Kondo lattice with partial frustration* in *Journal of Physics: Conference Series* **807** (2017), 032003.

55. Kitazawa, H., Matsushita, A., Matsumoto, T. & Suzuki, T. Electronic and thermal properties of CePdAl. *Physica B: Condensed Matter* **199,** 28–30 (1994).

56. Fang, C. *et al.* New insight into magneto-structural phase transitions in layered TbMn2Ge2-based compounds. *Scientific Reports* **7,** 45814 (2017).

57. Gopal, E. *Specific heats at low temperatures* (Springer Science & Business Media, 2012).

58. Kneidinger, F. *Non-centrosymmetric superconductivity of intermetallic compounds in absence of strong correlations among electrons* PhD thesis (Technische Universität Wien, 2014).

59. Mugiraneza, S. & Hallas, A. M. Tutorial: a beginner's guide to interpreting magnetic susceptibility data with the Curie-Weiss law. *Communications Physics* **5,** 95 (2022).

60. Bustingorry, S., Pomiro, F., Aurelio, G. & Curiale, J. Second-order magnetic critical points at finite magnetic fields: Revisiting Arrott plots. *Physical Review B* **93,** 224429 (2016).

61. Taufour, V., Hodovanets, H., Kim, S. K., Bud'ko, S. L. & Canfield, P. C. Electrical resistivity study of CeZn 11: Magnetic field and pressure phase diagram up to 5 GPa. *Physical Review B—Condensed Matter and Materials Physics* **88,** 195114 (2013).

62. Fu, L. *et al.* High-pressure synthesis and characterizations of a new ternary Ce-based compound Ce3TiAs5. *Journal of Physics: Condensed Matter* **37,** 015803 (2024).

63. Wang, K., Wei, W. & Du, H. The Cubic B20 Chiral Magnet FeGe. *Advanced Functional Materials* **35,** 2416203 (2025).

64. Nakajima, T. *et al.* Skyrmion lattice structural transition in MnSi. *Science advances* **3,** e1602562 (2017).

65. Münzer, W. *et al.* Skyrmion lattice in the doped semiconductor Fe 1- x Co x Si. *Physical Review B—Condensed Matter and Materials Physics* **81,** 041203 (2010).

66. Bauer, A. & Pfleiderer, C. Magnetic phase diagram of MnSi inferred from magnetization and ac susceptibility. *Physical Review B—Condensed Matter and Materials Physics* **85,** 214418 (2012).

67. Turgut, E., Stolt, M. J., Jin, S. & Fuchs, G. D. Topological spin dynamics in cubic FeGe near room temperature. *Journal of Applied Physics* **122** (2017).

68. Leroux, M. *et al.* Skyrmion lattice topological Hall effect near room temperature. *Scientific reports* **8,** 15510 (2018).

69. OpenAI, D. Online. For linguistic improvements and text formulation, the AI models DeepL Write and ChatGPT were utilized. 2025.

Appendix

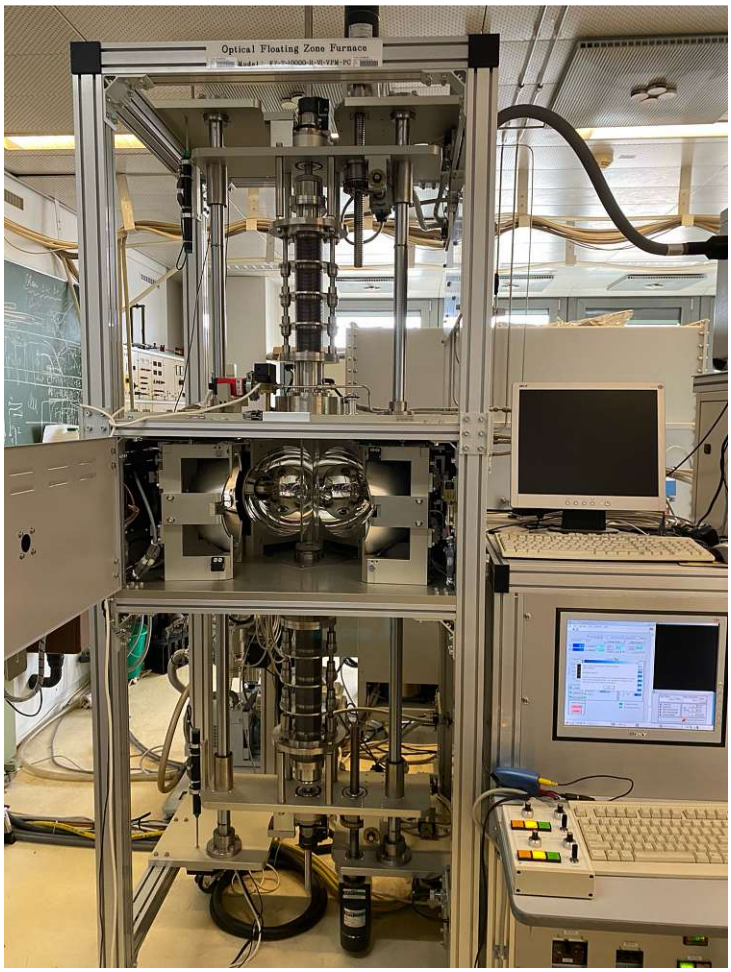

Figure A.1: Experimental setup for the TFZ method

Acknowledgements

First and foremost, I would like to express my deepest gratitude to my supervisor, Dr. Xinlin Yan, for his guidance and patience throughout my research journey. He not only showed me the importance of working accurately, cleanly, and efficiently but also imparted valuable life lessons drawn from Chinese tradition.

I would also like to express my sincere gratitude to Dr. Andrey Prokofiev, whose valuable advice after every new set of measurement results was always insightful. I thoroughly enjoyed our discussions, and they greatly enriched my research. I especially appreciate

his years of experience and the wealth of knowledge he has accumulated over the years.

Furthermore, I would like to thank Dr. Silke Bühler-Paschen for the incredible opportunity to conduct this research. Her support and the resources provided were essential in making this research possible.

Additionally, I would like to express my gratitude to the members of the Quantum Materials Group, especially Dr. Duy Ha Nguyen and Nikolas Reumann for his assistance with the dilution refrigerator, Mrs. Monica Waas for her invaluable support with the EDX and SEM measurements, and Mrs. Angelika Bosak for her organizational assistance.

Finally, I would like to express my gratitude to all my family and friends, whose support has been invaluable throughout the years. Their encouragement, both in times of challenge and success, has kept me motivated. I am especially grateful to my parents, who have always been a pillar of strength, providing not only financial support but also constant moral encouragement. Their belief in me has been a foundation upon which I could rely, and I could not have completed this journey without them.

I gratefully acknowledge financial support from the ERC Advanced Grant CorMeTop, which made this research possible.